2022-06

DETERMINATION OF A FREE-PISTON STIRLING ENGINE-GENERATOR OPERATING CURVE FOR APPLICATIONS IN ENERGY EXTRACTION

Nguyen, Sarah M.

Monterey, CA; Naval Postgraduate School

NAVAL POSTGRADUATE SCHOOL

MONTEREY, CALIFORNIA

THESIS

DETERMINATION OF A FREE-PISTON STIRLING ENGINE-GENERATOR OPERATING CURVE FOR APPLICATIONS IN ENERGY EXTRACTION

by

Sarah M. Nguyen

June 2022

Thesis Advisor:	Anthony G. Pollman
Co-Advisor:	Anthony J. Gannon
Second Reader:	Alejandro S. Hernandez

THIS PAGE INTENTIONALLY LEFT BLANK

REPORT DOCUMENTATION PAGE			*Form Approved OMB No. 0704-0188*

1. AGENCY USE ONLY *(Leave blank)*	**2. REPORT DATE** June 2022	**3. REPORT TYPE AND DATES COVERED** Master's thesis

4. TITLE AND SUBTITLE
DETERMINATION OF A FREE-PISTON STIRLING ENGINE-GENERATOR OPERATING CURVE FOR APPLICATIONS IN ENERGY EXTRACTION

5. FUNDING NUMBERS
RMQ80

6. AUTHOR(S) Sarah M. Nguyen

7. PERFORMING ORGANIZATION NAME(S) AND ADDRESS(ES)
Naval Postgraduate School
Monterey, CA 93943-5000

8. PERFORMING ORGANIZATION REPORT NUMBER

9. SPONSORING / MONITORING AGENCY NAME(S) AND ADDRESS(ES)
Office of Naval Research, Arlington, VA 2203–1995

10. SPONSORING / MONITORING AGENCY REPORT NUMBER

11. SUPPLEMENTARY NOTES The views expressed in this thesis are those of the author and do not reflect the official policy or position of the Department of Defense or the U.S. Government.

12a. DISTRIBUTION / AVAILABILITY STATEMENT
Approved for public release. Distribution is unlimited.

12b. DISTRIBUTION CODE
A

13. ABSTRACT (maximum 200 words)

Renewable energy generation faces challenges in energy storage, particularly in providing sustained load management between periods of excess generation, peak demand, and intermittency. Clean and dependable energy storage methods exist, but the need for higher efficiency energy extraction motivates the search for sophisticated methods. One such method is a Liquid Air Energy Storage (LAES) system paired with a Stirling engine. This thesis investigated the power output of a particular Free-Piston Stirling Engine-Generator (FPSEG) for potential use in energy extraction from the aforementioned system to power an islanded microgrid. A full FPSEG testing apparatus was constructed and several heating conditions were tested to obtain an operating curve for the studied FPSEG. Additionally, a basic numerical model was developed for the FPSEG working fluid. Data from these experiments were evaluated to show potential coupling capabilities with a LAES system.

14. SUBJECT TERMS
Stirling engine, renewable energy generation, LAES, liquid air energy storage, FPSEG, Free-Piston Stirling Engine-Generator

15. NUMBER OF PAGES
121

16. PRICE CODE

17. SECURITY CLASSIFICATION OF REPORT	**18. SECURITY CLASSIFICATION OF THIS PAGE**	**19. SECURITY CLASSIFICATION OF ABSTRACT**	**20. LIMITATION OF ABSTRACT**
Unclassified	Unclassified	Unclassified	UU

NSN 7540-01-280-5500

Standard Form 298 (Rev. 2-89)
Prescribed by ANSI Std. 239-18

THIS PAGE INTENTIONALLY LEFT BLANK

Approved for public release. Distribution is unlimited.

DETERMINATION OF A FREE-PISTON STIRLING ENGINE-GENERATOR OPERATING CURVE FOR APPLICATIONS IN ENERGY EXTRACTION

Sarah M. Nguyen
Ensign, United States Navy
BS, United States Naval Academy, 2021

Submitted in partial fulfillment of the
requirements for the degree of

MASTER OF SCIENCE IN MECHANICAL ENGINEERING

from the

NAVAL POSTGRADUATE SCHOOL
June 2022

Approved by: Anthony G. Pollman
Advisor

Anthony J. Gannon
Co-Advisor

Alejandro S. Hernandez
Second Reader

Garth V. Hobson
Chair, Department of Mechanical and Aerospace Engineering

THIS PAGE INTENTIONALLY LEFT BLANK

ABSTRACT

Renewable energy generation faces challenges in energy storage, particularly in providing sustained load management between periods of excess generation, peak demand, and intermittency. Clean and dependable energy storage methods exist, but the need for higher efficiency energy extraction motivates the search for sophisticated methods. One such method is a Liquid Air Energy Storage (LAES) system paired with a Stirling engine. This thesis investigated the power output of a particular Free-Piston Stirling Engine-Generator (FPSEG) for potential use in energy extraction from the aforementioned system to power an islanded microgrid. A full FPSEG testing apparatus was constructed and several heating conditions were tested to obtain an operating curve for the studied FPSEG. Additionally, a basic numerical model was developed for the FPSEG working fluid. Data from these experiments were evaluated to show potential coupling capabilities with a LAES system.

THIS PAGE INTENTIONALLY LEFT BLANK

TABLE OF CONTENTS

LIST OF FIGURES

LIST OF TABLES

THIS PAGE INTENTIONALLY LEFT BLANK

LIST OF ACRONYMS AND ABBREVIATIONS

ECE	external combustion engine
FPSE	free-piston Stirling engine
FPSEG	free-piston Stirling engine-generator
ICE	internal combustion engine
LAES	liquid air energy storage

THIS PAGE INTENTIONALLY LEFT BLANK

ACKNOWLEDGMENTS

I would like to extend a huge thanks to my advisors, Dr. Pollman and Dr. Gannon. I am truly thankful for the guidance that they have offered me throughout this entire process and for the time they have invested into making me a better student and person. I will carry the lessons and experiences they have given me into the next phase of my life and am grateful for what I was able to learn from them at NPS. I would also like to give a special thanks to John Gibson and Dave Dausen, who have done so much to support me and my goals for this thesis. I cannot thank them enough, and I owe the success of this thesis to their kindness and help. Last and not least, I want to thank my family, friends, and roommates for all of the support that they have given me this last year. I could not be more grateful for the kindness and support that they have shown me in every circumstance and could not have done anything without them.

THIS PAGE INTENTIONALLY LEFT BLANK

I. INTRODUCTION

A. BACKGROUND AND MOTIVATION

Electrical power is a fundamental commodity needed to enable all functions of modern societies in the world. With the current and increasing energy demands of nations and the depletion of fossil fuels continually driving costs upward, global interest in electrical generation has shifted toward the assimilation of renewable energy sources to power the world's grid systems. In addition to economic pursuits, the burning of fossil fuels is known to cause long-term environmental damage. To combat this, current projections show that 22% of the United States' anticipated energy generation will be from renewable energy sources this year, reducing the amount of energy produced by natural gas and other fossil fuels [1]. Furthermore, policy in the United States aggressively aims to achieve a carbon-free and pollution-free electricity generation sector by 2030, and a zero-emissions economy by 2050 [2], [3]. Over the last two decades, these motivations have caused a surge in interest in the search for clean and affordable methods to generate and store power.

Renewables are most often used in today's microgrid systems. A microgrid is a controllable power network that consists of its own energy generation capabilities. These microgrids can operate either in tandem with the main power grid or independently as an islanded system. They offer numerous benefits to include greater control over distribution according to generation and demand, minimal transmission losses compared to main grid dissemination, increased resiliency and emergency power generation to the main grid, and the capability to employ renewable and zero-emission electricity sources [4].

When paired with renewables, however, these microgrids face key challenges: sustained load stability and the need for clean energy storage. Renewable energy sources, such as photovoltaic cells and wind turbines experience intermittent periods of generation based off their reliance on nature. For example, a period when there is a lack of sunlight prohibits solar panels to collect and supply solar energy. Similarly, a period of low wind speed would also imply low generation for a wind farm. As a result, the natural fluctuation

of energy availability means that the power supplied by renewables is inherently infrequent. This leads to issues in load stability, since renewables cannot reliably supply energy as immediately as the demand rises, nor is the power easily adjustable to consumer needs [5]. Thus, for microgrids to provide sustained energy during periods of intermittency, and to provide a more efficient means of load management, energy storage systems are of critical importance. Storage systems provide a certain capacity for energy to go during periods of low demand or overproduction. This helps to resolve the load shedding issue, and ensures that energy is available during peak demand, when it is most valuable [6]. While batteries and supercapacitors are the most commercially used methods of storage, they are known to produce undesirable byproducts and degrade over time—even if not in use [7]. Additionally, lead-acid batteries are unable to withstand high cycling rates, and have a low storage capacity for their volume [6]. Energy storage methods such as liquid air cryogenics and supercapacitor banks are the subjects of extensive research in the energy community. However, these storage methods can only operate as well as their capability to receive and extract energy. To achieve resilience and sustained energy dissemination during periods of power intermittency, low demand, and peak load, a clean and reliable method of energy storage and extraction must be implemented.

B. STIRLING CYCLE ENERGY EXTRACTION

The method of interest of energy extraction in this study is the free-piston Stirling engine-generator (FPSEG). The Stirling engine, based on the thermodynamic Stirling Cycle, is a device that converts thermal energy into mechanical work, which can then be used to generate electrical power [8]. It is closed-fluid external combustion engine, meaning that it can operate using any type of heat source, conventional or non-conventional – e.g. combusted gases, solid fuels, solar energy, waste and exhaust heat, and more [8]. This ability to take advantage of any type of heat source makes Stirling engines an extremely versatile method of energy generation, and allows them to be easily paired with renewable and clean energy sources. Additionally, Stirling engines can have thermal efficiencies as high as their Carnot efficiencies [8], [9]. The Carnot efficiency is defined in Equation 1, and will be described in further detail in Chapter II, Section A.2.

$$\eta_{Carnot} = 1 - \frac{T_C}{T_H} \quad (1)$$

T_C and T_H are the temperatures of the cold sink and hot source, respectively. When a system operates at its Carnot efficiency, it means that the system is capable of operating at the highest achievable efficiency for a thermodynamic state. These advantages make the Stirling engine a prime candidate in the energy extraction crisis, especially when combined with a reliable means of energy storage.

C. THESIS OVERVIEW

This study is part of a larger research effort to integrate a Stirling engine with a liquid air energy storage (LAES) system connected to a microgrid. In this system, excess generated energy from the grid is used to compress and liquify air, which is stored in containers at standard temperature and pressure conditions. When power is needed, the liquid air is run through the Stirling engine as a coolant. The temperature difference created between the cryogenic coolant and the ambient air drives the Stirling cycle, by which electrical power is generated. For the proposed LAES-FPSEG system, the expected T_H for room temperature is 288.5 K and the expected T_C is 78 K—the temperature required for air to remain a liquid at atmospheric pressure [10]. Under these thermal conditions, the expected Carnot efficiency is calculated as 72.97 %. The potential for this high thermal efficiency is what draws great interest to FPSEGs.

The FPSEG intended for this system has not yet been tested for this application. Thus, the scope of this thesis is concerned with investigating the Stirling engine chosen for this system—the Microgen Hanging Gas Engine. In this thesis, various heating and cooling conditions were applied to this FPSEG for the purpose of constructing an operating curve relating the electrical power output to numerous temperature differences. Data from this study was used to inform future efforts in FPSEG energy extraction, and how much power is expected when coupled to various energy storage systems. This thesis explored this relationship using two methods: a computational analysis and an experimental demonstration.

First, a simulation was constructed using ANSYS Fluent to characterize the gas dynamics and heat transfer occurring cyclically in an FPSEG. An initial model, based off an FPSEG with known parameters was used in an effort to validate the computational methods developed. A validated model could be applied to the current FPSEG to obtain a computationally informed estimate of the engine's power output for an array of heat sources and sinks.

Next, an experiment was conducted to test and record the power output of the generator for a set of temperature differences, achieved by increasing the thermal energy input of the heating system.

The data gathered from both the computational and experimental efforts were analyzed. Consistent results between the model and experiment would allow for extrapolation methods to be used to estimate engine power output beyond the bounds of the original experiments.

II. LITERATURE REVIEW

A. STIRLING ENGINE OVERVIEW

Unlike an automobile engine, which is an internal combustion engine (ICE), the Stirling engine is an external combustion (ECE) heat engine. The most prominent example of early external combustion engines to be commercialized was the steam engine of the 1800s. The steam engine used the heat from burning coals to boil water and produce steam, which was then circulated through a series of pipes and valves to push against a piston. The force exerted on the piston could then drive a wheel, transferring the original heat energy into rotational motion. The remaining steam was then exhausted through a valve, creating a smokestack. Though the steam engine could operate at high power outputs, it had three key issues. First, because the boiler was a distance away from the power piston, heat was being lost in transit. Second, the steam engine consumed a significant amount of steam and fuel during each cycle compared to the power output. Finally, much of the steam from the smokestack exhausted at high temperature, meaning there was a great amount of energy lost to the surroundings [11], [12]. In summary, the steam engine, though powerful, was inefficient, and had many key areas to be improved upon. These were the primary driving points that motivated the development of alternative engines, one of which was the Stirling engine, built shortly after the advent of the steam engine. Figure 1 shows an illustration of the original Stirling engine patent.

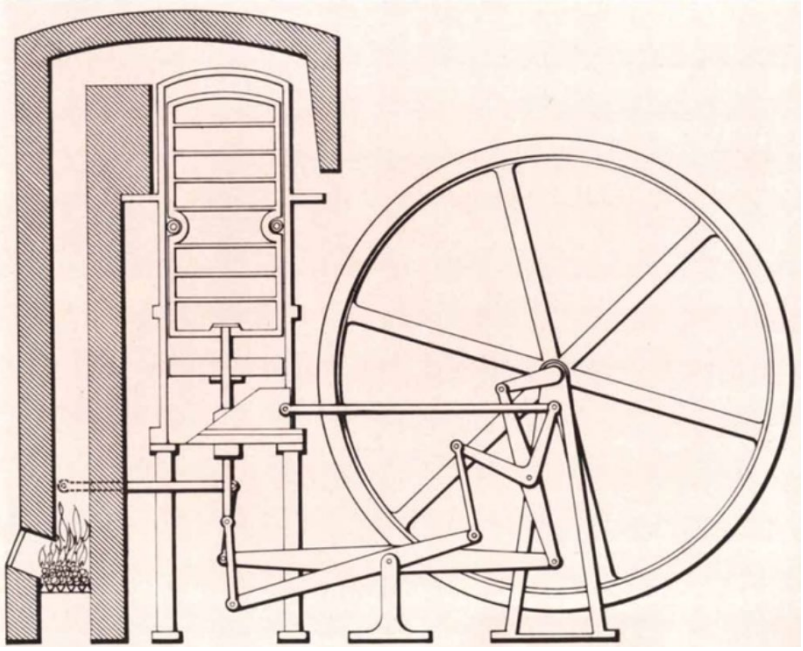

Figure 1. Original Stirling Engine Portrayal. Source: [13].

1. Brief History of Stirling Engines

The Stirling engine was first developed in 1816 by Robert Stirling, a Scottish clergyman whose goal was to resolve the safety and efficiency issues of the steam engine. Though the Stirling engine was also an external combustion engine, it had many key differences. The Stirling engine is a closed-cycle regenerative heat engine. As a heat engine, it converts energy from a heat flow into mechanical work. By using this energy flow, a Stirling engine can receive heat, then siphon some of it into mechanical work while the rest of it is rejected to the heat sink. This thermodynamic process is explained in greater detail in sections A.3 and A.4. The next large difference is that the Stirling engine has a closed cycle, which refers to the engine's working fluid. Unlike the steam engine or automobile ICE, the working fluid in a Stirling engine is completely sealed within the system and is used to transfer heat repeatedly for every cycle. Finally, the Stirling engine is regenerative, which means that some of the heat for each cycle is stored during one phase of the cycle and then recovered by the working fluid in a later phase by using a heat exchanger. This minimizes loss that would otherwise be exhausted, increasing the overall efficiency of the cycle [8], [11], [12]. The Stirling engine as a commercialized device has

since been dismissed with the development of ICEs (e.g. Otto and Diesel engines) dominating the industry since the 1860s. However, new interests in Stirling engines have taken root, as their high efficiencies and potential to couple with renewable energy resources have become a global interest in recent years.

2. Stirling Engine Components

There are many configurations of Stirling engines that exist today, but the primary components consist of a power piston, displacer piston, heating source, cooling source, regenerator, and working fluid, which today is often helium or nitrogen gas [14]. Figure 2 shows the basic components for a Stirling engine with a beta-type configuration. This particular configuration is characterized by a single-cylinder assembly with two mechanically-linked pistons that oscillate out of phase.

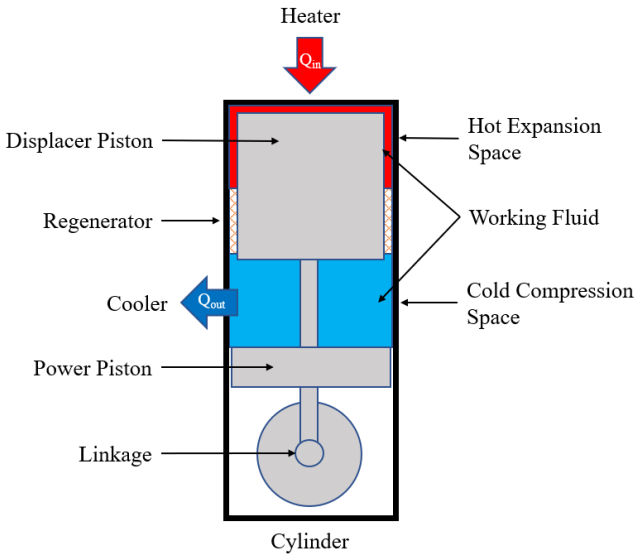

Figure 2. Components Diagram of a Beta Configuration Stirling Engine.

a. The Power Piston

The power piston is the component responsible for the final power output of the engine. The working fluid expands and contracts against this rigid surface, creating linear

oscillating motion with each cycle. When this motion is mechanically or magnetically linked to a generator, electrical power is produced.

b. The Displacer Piston

The displacer piston is responsible for shuttling the working fluid between the hot expansion and cold compression spaces through the indicated channel in Figure 2. This piston is only meant for the movement of the working fluid, and as a consequence, also oscillates up and down. However, no net work exerted on this piston or by this piston.

c. Heating and Cooling Sources

Because Stirling engines are external combustion engines and need only a sustained temperature difference to operate, an extensive variety of heating and cooling combinations may be used. Examples of common heat sources include solar energy, combusted gases, bio-pellets, hot coals, and exhaust heat from other systems. Common cooling sources include water, ice, or even ambient air. The appropriate method of heating and cooling for a particular Stirling engine depends on the size of the engine [14]. Engines with greater power outputs require a greater temperature differential, while engines with smaller power outputs require a smaller one.

d. Regenerators

Regenerators are a type of heat exchanger internal to the engine, often made up of a porous or mesh material. Its purpose is to allow for the working fluid to alternate between its maximum high temperature state and minimum low temperature state without supplemental heat addition or removal provided by the heater and cooler [9], [15]. In doing so, regeneration increases the thermal efficiency of the system by storing heat that would otherwise be rejected to the surroundings and recovering it in the next cycle, effectively recycling thermal energy. This regenerative process occurs between the isothermal expansion and compression phases, which will be explained in greater detail in section A.4.

e. Working Fluid

It is advantageous to use a gas with low molecular weight and high thermal conductivity compared to air. This is because high conductivity will best promote heat transfer and improve efficiency. Water is the most common working fluid in closed loop systems, as it possesses a high heat capacity, high thermal conductivity, is abundant in nature, and can be combined with ions or other doping mechanisms to improve performance. Other closed loop heat transfer systems include molten salts, phase changing materials, and paraffins. Stirling engines could adapt to a wide variety of working fluids, but water is most common.

3. Heat Engine Principles

Before introducing the thermodynamic process of the Stirling Cycle, it is first important to review principles of heat engines.

An engine is a device that converts a source energy into mechanical energy which can then be used for work. They are generally categorized by the type of input energy used—this includes heat, chemical potential energy, electrical potential energy, nuclear energy, and more. In particular, heat engines take advantage of the natural energy flow that occurs when a working substance is brought from a higher temperature state to a lower one. Consistent with the Second Law of Thermodynamics, this heat flow depends on being able to maintain this constant temperature differential between isolated source and sink. First, thermal energy is added to the working substance, raising its temperature. Next, processes within the engine use the physical properties of the working substance to convert its thermal energy into mechanical work, which is the net output of the engine. As a result, the thermal energy of the working substance decreases, lowering its final temperature state. The working substance is often a fluid, and must have a heat capacity for this process to be used. The energy balance of this process is shown in Figure 3.

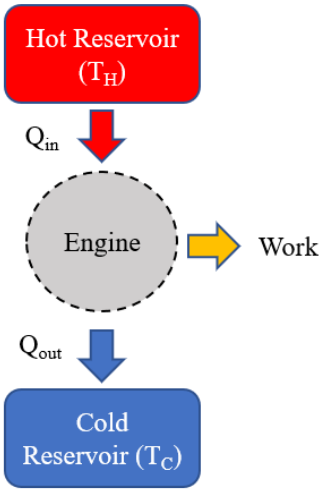

Figure 3. Heat Engine Energy Flow Diagram.

Figure 3 shows the energy flowing through the system, where Q_{in} and Q_{out} represent the heat input and output, respectively. Applying the First Law of Thermodynamics, which states that energy must be conserved, the following energy balance describes the basic heat engine:

$$Q_{in} = Work + Q_{out} \tag{1}$$

Rearranging this energy balance gives the definition of the output work of the engine:

$$Work = Q_{in} - Q_{out} \tag{2}$$

Thus, the net work produced by any heat engine is the difference between the initial heat added to the system and the leftover heat released to the surroundings. The thermal efficiency of a heat engine is expressed as follows in Equation 3.

$$\eta_{th} = \frac{Work}{Q_{in}} = \frac{Q_{in} - Q_{out}}{Q_{in}} = 1 - \frac{Q_{out}}{Q_{in}} \tag{3}$$

Efficiency, then, is defined as the ratio of the desired output of the engine (work) to the energy costs required to achieve it (heat addition). The more effectively an engine can extract usable energy from the input heat, the greater its thermal efficiency.

As mentioned previously, a fraction of the total energy is lost to the surroundings or converted to unusable forms of energy, like friction or drag. Because of this, heat engines are inherently unable to reach 100% efficiency, and are limited by what is called the Carnot efficiency. The Carnot efficiency is the theoretical maximum efficiency an engine can achieve using a working fluid for a given hot and cold temperature state. It assumes that heat is transferred isothermally between the source and sink. Thus, the Carnot efficiency is expressed explicitly on the basis of these temperatures, where T_H is the hot source temperature, and T_C is the cold sink temperature. The Carnot efficiency, previously defined in Equation 1, is repeated here.

$$\eta_{Carnot} = 1 - \frac{T_C}{T_H} \tag{4}$$

4. The Ideal Stirling Cycle

Figures 4 and 5 illustrate the thermodynamic cycle of a basic Stirling engine in the single-cylinder beta configuration, which consists of one power piston and one displacer piston to shuttle the working fluid between the expansion space and compression space.

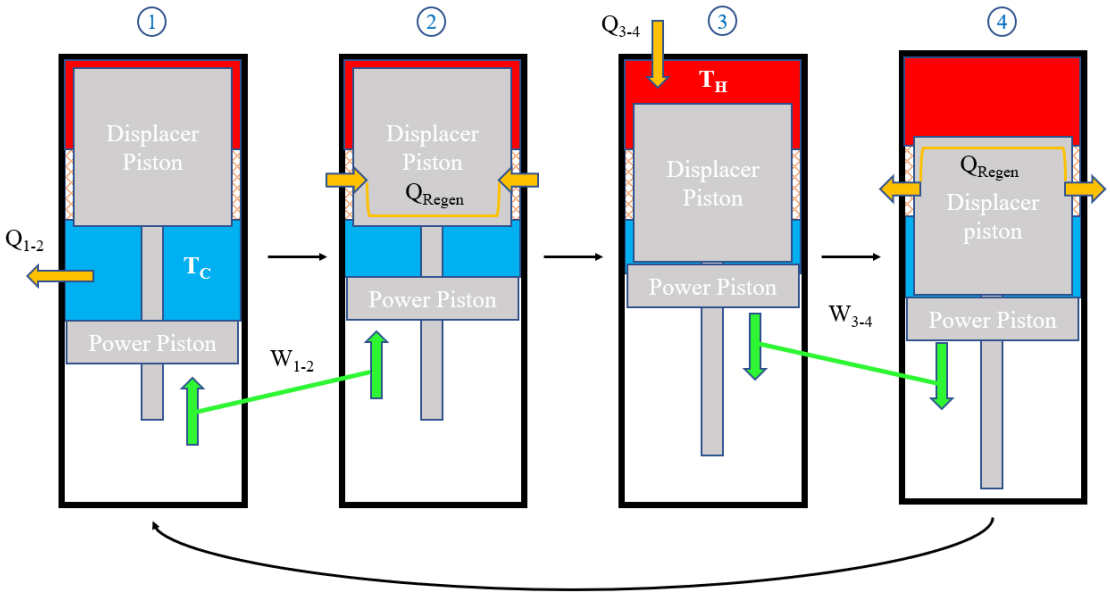

Figure 4. Stirling Cycle Piston-Cylinder Diagram.

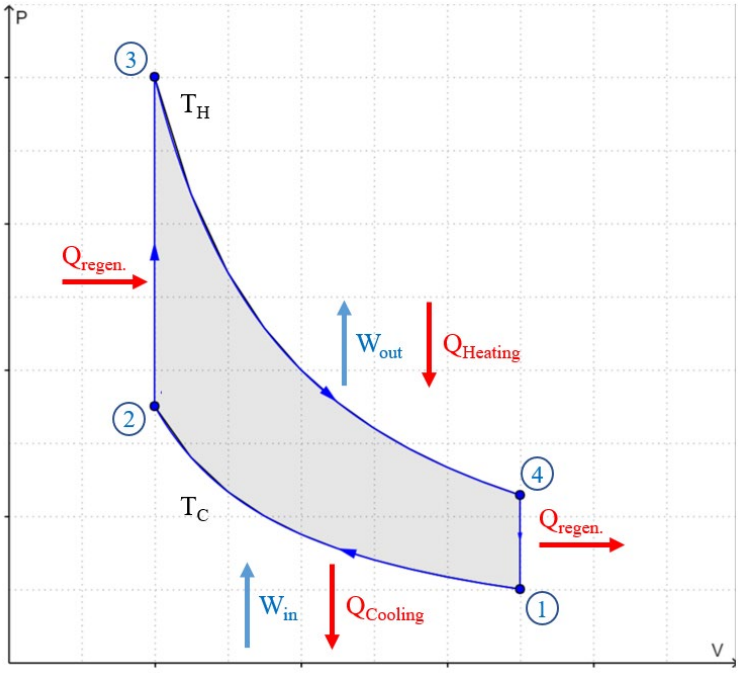

Figure 5. Ideal Stirling Cycle Pressure-Volume Graph.

The ideal Stirling Cycle consists of four distinct thermodynamic processes, as shown in Figure 5 [9], [16]. For reference, the cycle begins when the displacer piston is at

the top of its stroke, and a majority of the working fluid is in the cold compression space. Process 1-2 is the isothermal (constant temperature) compression of the cold volume. During this process, heat ($Q_{Cooling}$) is removed from the working fluid by the cold source, allowing it to maintain a constant temperature (T_C) as pressure increases and volume decreases. The total work (W_{in}) required to compress the fluid is the area under the P-V curve from state point 1 to 2, as in Equation 5.

$$W_{in} = \int_1^2 PdV = mRT_C \int_1^2 \frac{dV}{V} = mRT_C \; ln\left(\frac{V_2}{V_1}\right) \tag{5}$$

Process 2-3 is the isochoric (constant volume) regenerative heating and displacement of the working fluid from the cold compression space to the hot expansion space of the engine. Here, the working fluid passes through the regenerator and gains heat from the thermal energy stored from previous cycles. This heat addition, coupled with the heat source, raises the temperature of the fluid back to its maximum high temperature, T_H, by the beginning of state point 3. Because no work is done during this process, the heat added by the regenerator (Q_{Regen}) is equal to the change of internal energy of the fluid. Furthermore, because the working fluid is an ideal gas and its volume is unchanging, Equation 6 can be used to determine Q_{Regen}.

$$Q_{Regen} = \Delta U = mC_V \Delta T \tag{6}$$

Process 3-4 is isothermal expansion. Heat is continually added to the working fluid, enabling it to expand and exert work on the system. As pressure decreases and volume increases, continuous contact with the heat source keeps the working fluid at a constant temperature. The work exerted by the fluid is the area under the P-V curve from state point 3 to 4.

$$W_{out} = \int_3^4 PdV = mRT_H \int_3^4 \frac{dV}{V} = mRT_H \; ln\left(\frac{V_4}{V_3}\right) \tag{7}$$

Finally, process 4-1 is isochoric regenerative cooling and displacement of the working fluid from the hot expansion space back to the cold compression space. Similar to process 2-3, the volume of the fluid stays constant while its pressure changes—however,

heat in this process is now returned to the regenerator, resulting in a decrease in thermal energy of the fluid. Because the conditions of the fluid passing the regenerator are the same in this process as in process 2-3, the expression for the heat returning to the regenerator is equal to Equation 6, stated previously.

These four processes describe the complete Stirling Cycle. Further thermodynamic analyses allow the derivation of important cycle characteristics, such as the net work produced by the cycle and its thermal efficiency. To start, the 1st Law of Thermodynamics is applied to the system. Because the state of the working fluid does not have a net change between cycles, the change in internal energy for the cycle is equal to zero. Thus, Equation 8 is the describes the energy balance.

$$\Delta U = 0 = Q_{Regen} + Q_{Heating} - Q_{Regen} - Q_{Cooling} + W_{in} - W_{out} \quad (8)$$

Here, it important to note that for an ideal cycle, where TC and TH are constants, the heat given to the regenerator by the working fluid in process 4-1 is equal to the heat later recovered by the fluid in process 2-3. These values cancel over the course of a cycle, and Equation 8 reduces to Equation 9—the definition of W_{Net}.

$$W_{Net} = Q_{Cooling} - Q_{Heating} = W_{in} - W_{out} \quad (9)$$

Using the definition of thermal efficiency from Equation 3, the thermal efficiency for the ideal Stirling Cycle is expressed as follows:

$$\eta_{th_{Stirling}} = \frac{W_{Net}}{Q_{Heating}} = (1 - \frac{Q_{Cooling}}{Q_{Heating}}) \quad (10)$$

Because the ideal Stirling Cycle is thermodynamically reversible, the thermal efficiency is found to be equal to the Carnot efficiency, as defined in Equation 4.

5. Free-Piston Stirling Engines

A special type of Stirling engine which is investigated in this thesis is the free-piston Stirling engine (FPSE). The FPSE was first invented by Beale [11] in 1964. Though the original Stirling engine could theoretically reach Carnot efficiencies, the Beale engine design was the first to achieve the expected theoretical efficiencies. In the work of Beale,

the mechanisms of propagated loss that contributed to smaller efficiencies in traditional Stirling engines were described. The largest issue was the energy loss related to mechanical linkage of the pistons and crankshaft. Pressures exerted on the pistons by the working fluid were not perfectly in sync with the phase of the pistons as fixed by the linked driving mechanism. Additionally, there were constant issues with sealing tightness as well as lubrication, which meant that the engines had to be regularly maintained. Motivated by these performance gaps, the Free-Piston Stirling Engine was invented.

Figure 6 shows the original image from the FPSE patent of Beale. The Stirling engine of Beale resembled a beta-type configuration and consisted of a single cylinder which was positioned vertically in order to minimize frictional drag. Rubber bands were used to suspend the piston and displacer against gravity, which helped the self-starting mechanisms of the engine [5].

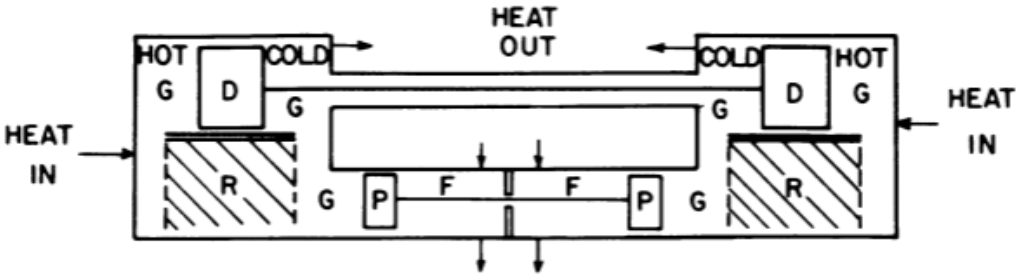

Figure 6. Original Free-Piston Stirling Engine. Source: [5].

The FPSE was a significant improvement to the traditional Stirling engine and had distinct difference. First, the Beale design directly addressed the frictional losses at the mechanical driving linkage by eliminating them completely. The Beale engine replaced this mechanism and the crankshaft with planar springs and magnets. The planar springs assisted in the reciprocating motion of the pistons, which meant that contact points for friction were greatly reduced. The magnets were attached to the power piston such that the oscillating motion of the piston, when coupled with a linear alternator, could replace the crankshaft to generate electrical power. More notably, this meant that the power and

displacer pistons were not linked together at all—thus, the phasing of the pistons were completely dependent on the gas dynamics of the working fluid. A lack of mechanical linkage and contact points also meant that lubrication was no longer necessary. This meant increased longevity and low maintenance, since oil would not degrade important components like the regenerator [5], [8], [17]–[19]. Additional benefits of the FPSE include low noise levels, low vibrations, ease in self-starting, and high thermal efficiencies [8].

B. MODELLING METHODS

Chen and Griffin [20] identified four Stirling engine design modelling methods: first-order, second-order, third-order, and the method of characteristics. Additional zeroth-order and fourth order methods are identified by Ridha et al. [21].

1. Zeroth-Order Analysis

Zeroth-order analysis includes methods first proposed by William Beale, whereby experimental data yielded correlations that could be used to empirically solve for power output [22]. These calculations involved what is called the Beale number, which related a FPSE's output power to pressure, operating frequency, and expansion space volume.

2. First-Order Analysis

a. The Isothermal Model

The isothermal model, known as Schmidt cycle analysis, was first demonstrated by Gustav Schmidt in 1871. Schmidt cycle analysis results in a closed form solution. Although it does not capture real cycle behavior, it is an improvement from ideal cycle analysis and the starting point of any further-developed real cycle models. Basic assumptions of the isothermal model are that the hot expansion space and cold compression space are maintained at a constant uniform temperature, equal to their respective maximum heat source and sink temperatures (T_H and T_C). These spaces are treated as single cells, connected by a non-isothermal regenerator. The regenerator is perfectly effective, and has a linear relationship over change in distance between the sink and source temperatures.

Finally, the piston motions are defined as a sinusoidal motion, whereby the phase of the displacer and power pistons are offset by an angle θ, as shown in Equations 11 and 12.

$$Y_{displacer} = A_{displacer} sin\,(\omega t) \tag{11}$$

$$Y_{power} = A_{power} sin\,(\omega t - \theta) \tag{12}$$

The constant temperatures of the expansion and compression spaces imply that all heat transfer is internal to the system—i.e. the regenerator is the only avenue of heat transfer between the spaces, and no heat escapes to the environment. As a result, it is found that over a cycle, the heat transferred between these bodies is exactly equal to the work done on the pistons, effectively making the heater and cooler redundant [23]. Though this model is an improvement to zeroth-order analysis, this result is not true of real engines, whereby there is net heat transfer over the cycle.

b. The Adiabatic Model

A more realistic first-order analysis remediates this issue by considering the heat transfer from the environment to the heater and cooler [20], [24]. This is known as the adiabatic model, which was developed by Finkelstein [25] in 1960. This model assumes an adiabatic expansion space, compression space, and regenerator. The heater and cooler are isothermal, as modelled by Schmidt cycle analysis, and receive (or reject) heat from the environment which is subsequently transferred to the expansion and compression spaces. Thus, the temperature of either volumes varies with the enthalpy flows associated with the adiabatic compression or expansion occurring throughout the cycle. This analysis captures the net heat transferred to and from the system, and is a more realistic FPSE model, compared to isothermal analysis. The solution requires simple numerical integration.

3. Second-Order Analysis

Second-order analyses are based off first-order methods, but improve the results by accounting for various loss terms, then adding them to the predicted net cycle performance. First, the basic work output is calculated from the isothermal or adiabatic model, then energy loss terms are subtracted from the output and thermal loss terms are added to the

input. These loss terms are decoupled, meaning that they are not dependent on each other. Thermal loss terms include imperfect heat transfer in the regenerator, working fluid shuttling loss, and conductive heat losses. Energy loss terms include pumping losses, fluid frictional losses, and energy density loss due to working fluid leakage [20], [21].

4. Third-Order Analysis

Third-order analysis considers that energy and thermal loss terms have a non-negligible effect on each other. These methods are also known as nodal analysis. The engine space is divided into a set of nodes, then fluid interactions are found in each node simultaneously by solving the differential equations of conservation of mass, energy, and momentum [20]. Numerical methods are used to obtain these solutions. Though this method is more sophisticated, it is not shown to be significantly more correct than solutions found suing second-order analyses.

5. Fourth-Order Analysis

Fourth-order analysis involves the use of computational fluid dynamic (CFD) codes. CFD offers a precise way to account for complex fluid interactions such as viscous effects, turbulence, kinetic interactions between molecules, and more. Recent CFD studies have successfully captures FPSE behaviors and have been used to inform potential design decisions on the component level of prototype FPSEs [26].

A particular study of interest conducted by Ridha et al. [21] demonstrated a simulation that could successfully capture the fluid-solid interactions in a complete Stirling cycle, and evaluate the total work produced by the engine. The system they studied was the Sunpower B-10 Stirling Engine. Prior to this work, most FPSE analyses did not include the fluid structure interactions between the working fluid and pistons. Thus, the goal of the study was to simulate the entire FPSE system from transient behavior to steady state, such that the motion of the power piston and displacer are affected by the thermodynamic solution of the working fluid. Ridha used ANSYS Fluent, and particularly, the six degrees of freedom solver (6DOF) to account for these interactions. Considerations for simulating this system included computing the external force of the working gas pressure and shear stress, the gravitational force acting on the displacer and power piston, and the spring force

on the power piston. Simulation results were compared to experimental results, as found in a study conducted by Saturno [27]. The comparison between Ridha's model and Saturno's work validated the 6DOF method as a tool to predict fluid-structure interactions in FPSEs.

C. CURRENT STATE OF THE ART

1. Waste Heat Recovery

Stirling engines have been shown to generate power with high efficiencies for low temperature thermal sources. This potential has drawn much attention to Stirling engines for applications in waste and exhaust heat recovery, which can operate between 100 °C and 500 °C depending on the size of the engine [28].

Durcansky et al. [29] investigated the use of the Cleanergy Stirling engine for waste heat recovery while evaluating operation at different temperatures and working fluid pressures. Using both experimental and numerical methods, they determined that the Cleanergy Stirling engine increased in power output for increasing temperature or pressure conditions. Simulations showed that while temperature increased from 300 °C to 800 °C and pressure remained constant, the net power output nearly doubled for each tested working pressure. Stronger dependence was shown in the working pressure trends—the net power output for a constant temperature was shown to increase in an approximately linear fashion as pressure rose. This engine was determined to be suitable for temperatures above 300 °C, indicating use with medium-range waste heat or solar sources.

2. Solar and Biomass Energy Recovery

Zhu et al. [30] demonstrated the successful integration of a FPSEG with a parabolic trough collector for solar power generation. For this application, low to mid-range temperatures were expected of the environment. The parabolic lens concentrated solar energy onto a receiver tube, which supplied thermal energy to the FPSEG. The FPSEG had a power rating of 5 kW, and the maximum power output for the expected temperature conditions was 3,000 W with a thermal-to-electric efficiency of 26.2% at 390 °C. Using solar energy, the maximum demonstrated power output was 2008 W at a heater head temperature of 300 °C and a thermal-to-electric efficiency of 15%. Inefficiencies were

identified as heat lost across the heat collection elements as well as the cosine loss, which related to the angle of incidence and corresponding irradiance. Optimization of design parameters to minimize these losses as well as the appropriate solar thermal insulation offers confidence that solar-integrated FPSEGs can achieve higher efficiencies and power outputs.

Mabe et al. [31] presented a hybrid power generation system composed of a biomass-burning FPSEG paired with a solar photovoltaic circuit and battery. By using these systems in tandem, the photovoltaic cell collected and stored solar energy during the day which was used to start the FPSEG and supply power to the controls box and other accessories. Meanwhile, the FPSEG generated power, which was also stored in the battery and provided a power source at night. Successful demonstration of the controls system allowed the heater head temperatures to be regulated between the operating limits identified as temperatures between 250 °C and 500 °C. Additionally, hot coolant water at 45 °C, when replaced in the system, was stored for uses such as cooking and cleaning. It was shown that the system could provide stable power output and could generate a maximum of 1,000 W and 200 L of hot water.

3. Liquid Air Energy Storage Extraction

A study conducted by Bailey [32] explored the viability of using Stirling engines as a method of energy recovery from a liquid air energy storage (LAES) system. A small beta-type Stirling engine, usually used for demonstrations, was used to generate power by inducing a high temperature difference on the engine with cryogenically liquified air and the surroundings. Bailey showed that under these thermal conditions, it was possible to generate electricity, however the energy output of the Stirling engine was significantly smaller than the total latent heat of the liquid air consumed. These losses in efficiency were attributed to imperfect heat transfer between the apparatus and the environment, as well as inefficiencies in the design and components [32]. More specifically, the cryogenic temperatures caused the working mechanisms in the engine to contract, such that more energy was spent to achieve normal component motion. Furthermore, Bailey identified the

importance of isolating the hot and cold sinks from each other in order to maintain a high temperature difference.

Further applications of Stirling engines for LAES is shown by Bailey et al. [33], whereby a Dual-Stirling Cycle Liquid Air Battery is proposed. This system uses a cryocooler to liquify and store air in a dewar at ambient pressure. When energy is needed, the cooled air is sent to a Stirling engine, which utilizes the temperature difference to produce work on the pistons and generates electricity.

THIS PAGE INTENTIONALLY LEFT BLANK

III. ANSYS FLUENT MODELLING METHODS

A. MODELLING APPROACH

The goal of this chapter is to develop a model of the fluid interactions in the studied FPSEG for various thermal conditions. A working model offers the advantage of being able to predict engine parameters for operating conditions not tested experimentally. The model is constructed first by verifying methods applied to an FPSE of known parameters and experimental behaviors. Once the modelling method is validated against experimental data, it is applied to the parameters of the FPSEG investigated in this study.

The FPSE chosen for the preliminary model is the Sunpower B-10 Stirling Engine. The Sunpower B-10 Stirling Engine features a beta configuration and uses air as the working fluid (Figure 7).

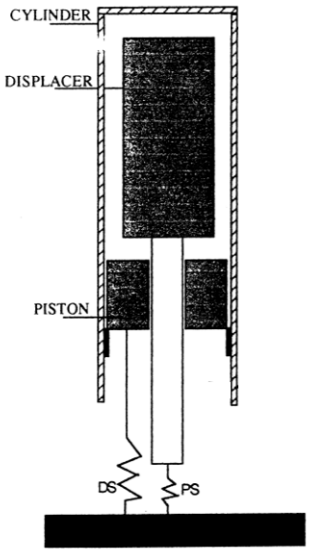

Figure 7. Sunpower B-10 Stirling Engine Schematic. Source: [27].

The simulation is modelled using ANSYS Fluent software (version 19.2), which has the ability to appropriately capture the dynamic motion of the pistons as well as the fluid-structure interactions between the pistons and working fluid. A dynamic mesh is applied such that the computational cells can respond to the motion of the pistons. Piston

movement is defined sinusoidally, consistent with Schmidt Cycle Analysis. Finally, a range of thermodynamic conditions is tested and compared to experimental results.

B. SUNPOWER B-10 MODEL SETUP

Table 1 shows the geometric and operating parameters for the Sunpower B-10.

Table 1. Sunpower B-10 Model Parameters. Source: [21], [27]

Parameter	Description	Value
D_p	Diameter of Power Piston	35.62 mm
D_d	Diameter of Displacer Piston	34.00 mm
D_r	Diameter of Connection Rod	12.65 mm
Dc	Diameter of the Cylinder	37.62 mm
t	Cylinder Wall Thickness	1.00 mm
L_p	Length of the Power Piston	70.40 mm
L_d	Length of the Displacer Piston	93.45 mm
L_{e0}	Initial Length of the Expansion Space	9.43 mm
L_{c0}	Initial Length of the Compression Space	20.50 mm
m_p	Mass of the Power Piston	0.5295 kg
m_d	Mass of the Displacer Piston	0.0867 kg
A_p	Amplitude of the Power Piston	5.30 mm
A_d	Amplitude of the Displacer Piston	6.40 mm
θ	Phase Angle Difference	60.81°
f	Cycle Frequency	77.43 rad/s
T_H	Hot Source Temperature	600 K
T_C	Cold Source Temperature	300 K

1. Geometry

In order to decrease the computation time, a 2D axisymmetric plane of the fluid domain is built in SolidWorks 2021. The geometry is split into three main bodies: the expansion zone, displacer channel, and the compression zone. Once these bodies are defined, they are saved as an assembly, allowing Fluent to recognize three separate domains once the body was imported. The purpose of defining separate domains is to be able to apply and isolate an inflation layer in the displacer channel without having to create excess meshed layers within the expansion and compression zones. Additionally, to

achieve appropriate mesh motion, it is necessary to define a horizontal surface cutting across the fluid plane where each of the pistons were expected to move: the top of the displacer, the bottom of the displacer, and the top of the power piston.

Finally, to define moving boundaries and create thermal conditions, the walls of the body are given names, as indicated in Figure 8.

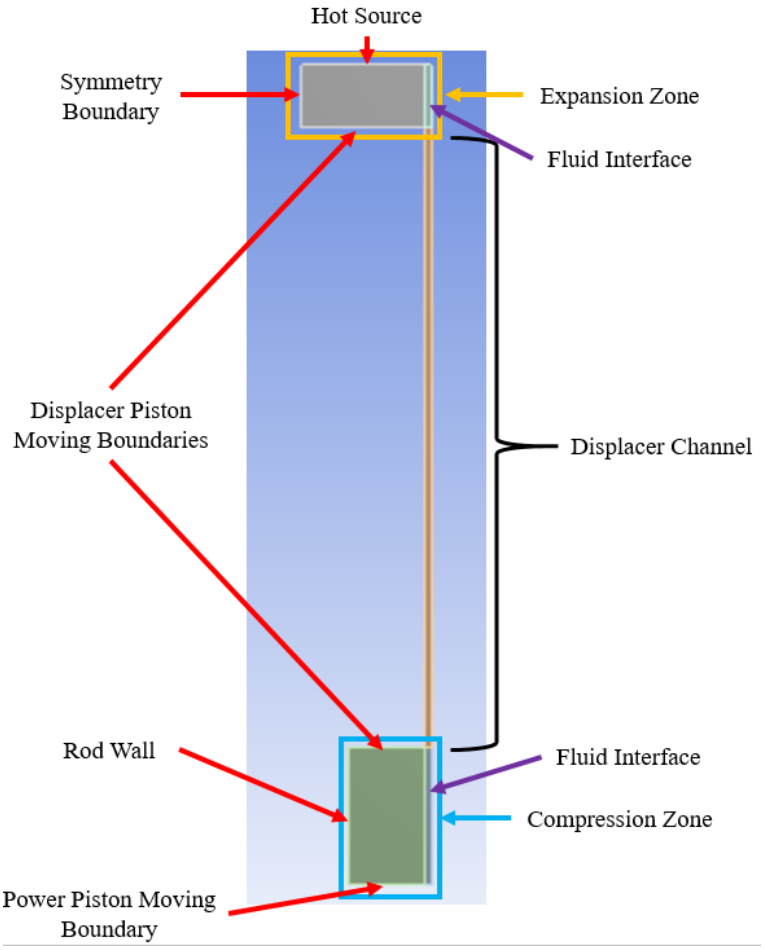

Figure 8. Model Geometry and Named Selections

2. Mesh Setup

Based off the expected fluid interactions and motion of the power and displacer pistons, certain mesh types are determined to be appropriate for each zone. Triangular cells of size 0.8 mm are applied to the expansion and compression zones. This made it easier to

deform these regions using the smoothing and remeshing functions, which will be described later. Next, the mesh in the displacer channel is defined as quadrilateral cells with a size of 0.1895 mm. By using this cell type, a uniform inflation layer can be applied, which captures the turbulent boundary layer occurring as fluid passes through the channel. The inflation zone has 6 layers with a first layer thickness of 1.1e-2 mm. The resulting mesh is shown in Figure 9 and had 9,142 nodes and 9,176 elements.

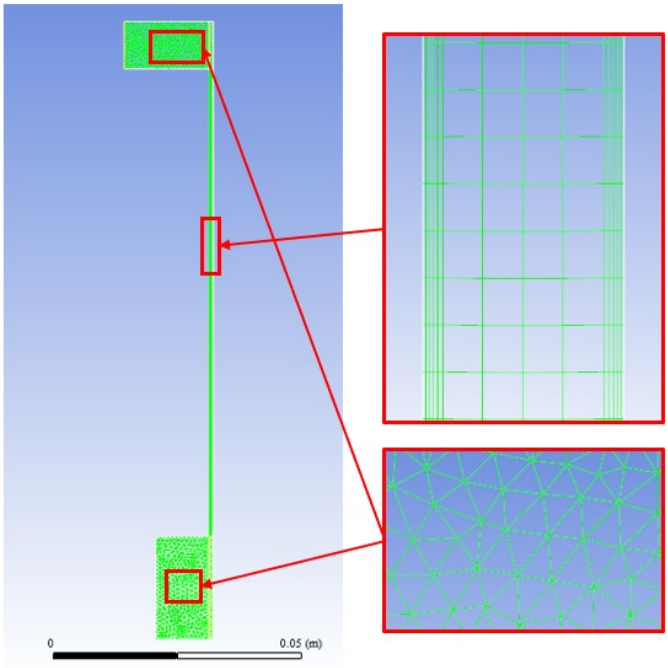

Figure 9. Model B-10 Mesh.

Next, a user-defined function is created to implement a velocity profile for each piston. Equations 11 and 12, from Schmidt Cycle Analysis, are used to model the piston and displacer profiles. The angular speed of the engine is 377 rad/s and the phase angle difference is 60.81°. These profiles are applied to the boundaries that represent the respective pistons. Under these conditions, the period of the cycle is 0.0167 seconds. The code used to define these motion profiles are recorded in Appendix A, and the resulting profiles are found in Appendix B.

Once moving boundaries are established, dynamic mesh methods are applied to each zone, enabling the total mesh to conform to the motion of the pistons. The methods used depended on the cell types in each zone. For the triangular cells in the expansion and compression spaces, the spring-based smoothing and remeshing methods are applied, and for the quadrilateral cells in the displacer channel, the layering method is applied. Additionally, the Rod Wall, Displacer Channel outer walls, Expansion Zone outer wall and Compression Zone outer walls are defined as "deforming" walls, which enabled them to deform to the movement of the cell zone boundaries.

3. Boundary Conditions

A transient study is applied to capture the initial movements of the pistons as heat was added to the working fluid. Next, the energy equation is enabled. In order to solve the instantaneous pressure and viscous forces that contributed to the force exerted on the pistons, the realizable k-ε turbulence model, based on the Navier-Stokes equations, is applied. Air was selected as the working fluid, and UDFs adapted from Ridha's work are written to model the specific heat, dynamic viscosity, and thermal conductivity with respect to temperature changes [10].

$$C_p = 1.9327 * 10^{-10}T^4 - 7.9999 * 10^{-7}T^3 + 1.1407 * 10^{-3}T^2 - 4.4890 * 10^{-1}T + 1.0575 * 10^3 \quad (13)$$

$$\mu = 8.8848 * 10^{-15}T^3 - 3.2398 * 10^{-11}T^2 + 6.2657 * 10^{-8}T + 2.3543 * 10^{-6} \quad (14)$$

$$\lambda = 1.5207 * 10^{-11}T^3 - 4.857 * 10^{-8}T^2 + 1.0184 * 10^{-4}T - 3.9333 * 10^4 \quad (15)$$

Thermal boundary conditions are applied on the walls where the expected heat source and coolant flow would be in contact with the cylinder. These boundaries are located at the walls Hot Source and Power Piston Moving Boundary, as indicated in Figure 8. The hot and cold boundary conditions are set to constant temperature walls, where the hot source was held at 600 K and the cold source was held at 300 K to mimic the expected operating conditions.

4. Solver Settings

A time step size of 5e-05 is used for 220 time steps. The volume-averaged temperature and pressure of the overall fluid body as well as the individual expansion zone, compression zone, and displacer channel are monitored and recorded. Additionally, the y-velocity of the fluid and the force exerted on the displacer and power piston surfaces are recorded. The final solver settings for this simulation is reported in Appendix C.

C. RESULTS

Preliminary simulation results were collected for the Sunpower B-10 model. Figures 10 through 15 show the pressure, temperature, volume, velocity, and force data collected for a single run of the simulation. The MATLAB code used to compile and plot these results is recorded in Appendix D.

Figure 10 shows a progression of contours of the y-direction velocity of the fluid throughout the simulation run. These images reflect successful piston motion, as it can be shown that the expansion and compression spaces change in volume according to the oscillating moving boundaries. Furthermore, the contours show successful communication of the working fluid dynamics between the expansion zone, channel, and compression zone.

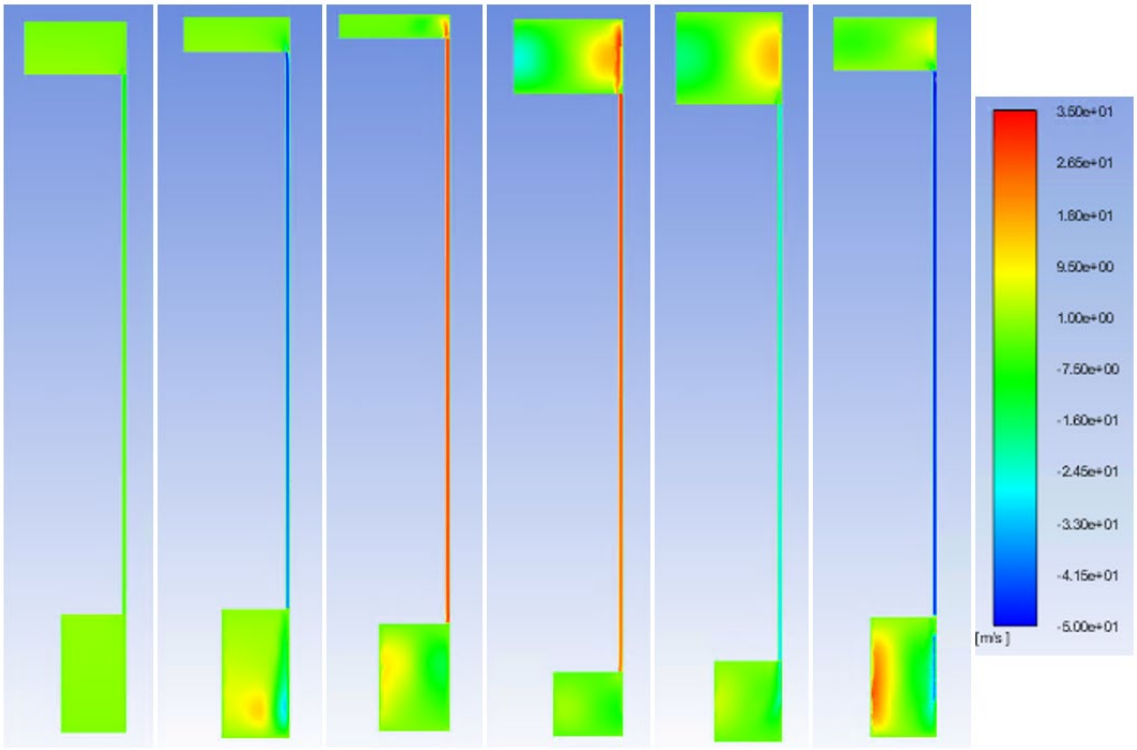

Figure 10. 6 Snapshots of Time-Progressive Y-Velocity Contours of the Working Fluid.

Figure 11 shows the average y-direction velocity over the boundaries interfacing between the channel and the respective expansion and compression zones. Interface 1 refers to the boundary at the expansion zone while interface 2 refers the boundary at the compression zone. These results further validate that the fluid was able to move between zone sections.

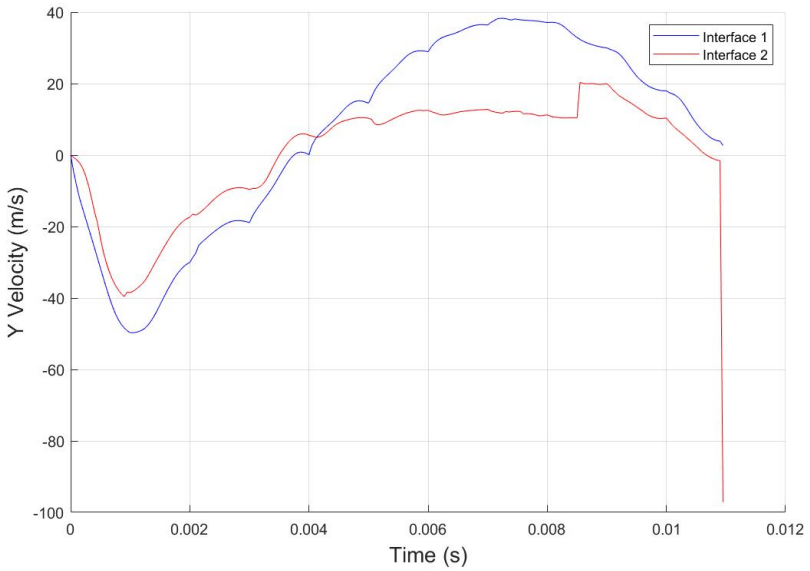

Figure 11. Y-Velocity of the Working Fluid at the Channel Interfaces.

Figure 12 shows the changing volumes of the total working fluid, expansion zone, and compression zone. As expected, these volumes increase and decrease sinusoidally, consistent with the motion profiles assigned to the pistons.

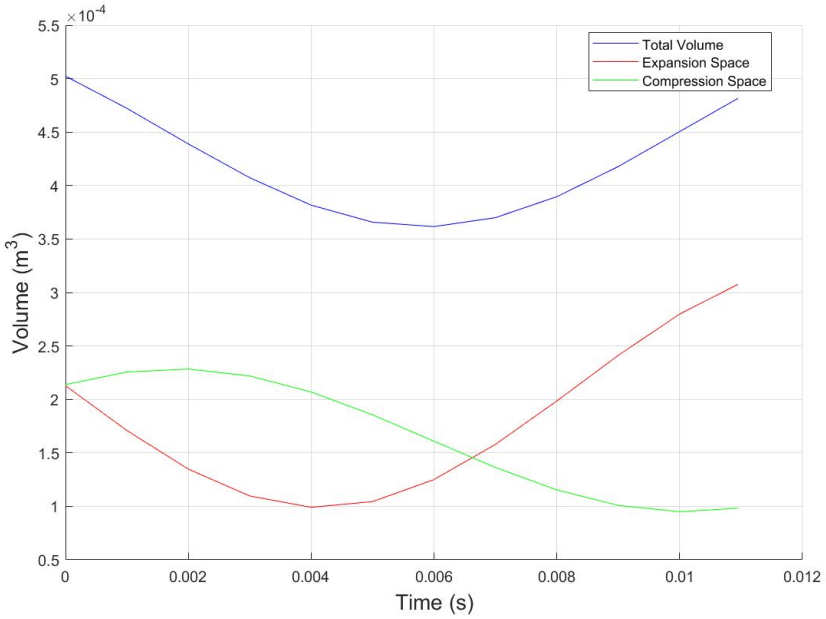

Figure 12. Plot of Engine Volumes Over Time.

Figure 13 shows the engine pressures over time. Consistent with the ideal gas law, the pressure of the working fluid at a given time is related to its volume, temperature, and density. Though the fluid is continually heated and cooled by the thermal boundaries, the overall pressure of the system and the respective expansion and compression zones increased and decreased in accordance with the total volume of the fluid. The point of maximum pressure is seen at 0.006 seconds, consistent with the point of minimum total volume in Figure 12. Small oscillations in pressure can be observed in the channel and expansion space. These oscillations are attributed to the movement of successively warm and cool fluid through the channel space and between the two volumes.

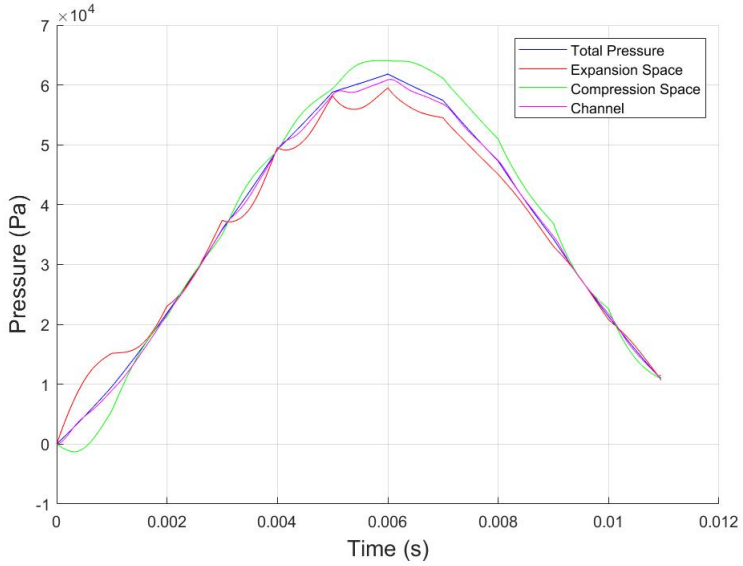

Figure 13. Plot of Engine Pressures Over Time.

Figure 14 shows the changes in temperature of the system over time. This trend is consistent with the pressure changes throughout the system. As expected, the expansion side experiences the warmest temperatures while the compression side experiences the coolest temperatures.

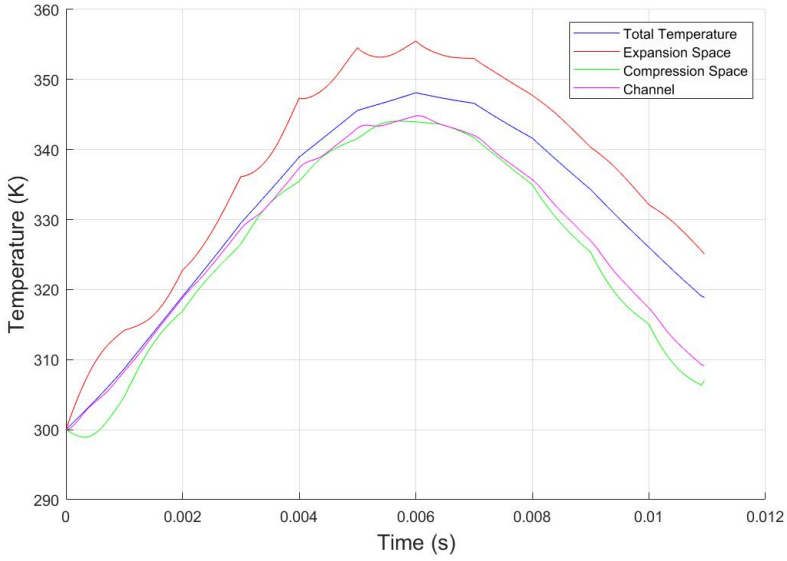

Figure 14. Plot of Engine Temperatures Over Time.

Figure 15 shows the average force on the fluid calculated over the displacer and power piston surface boundaries. The lower surface of the displacer piston is shown to experience inverse force effects to the power piston and upper surface of the displacer piston.

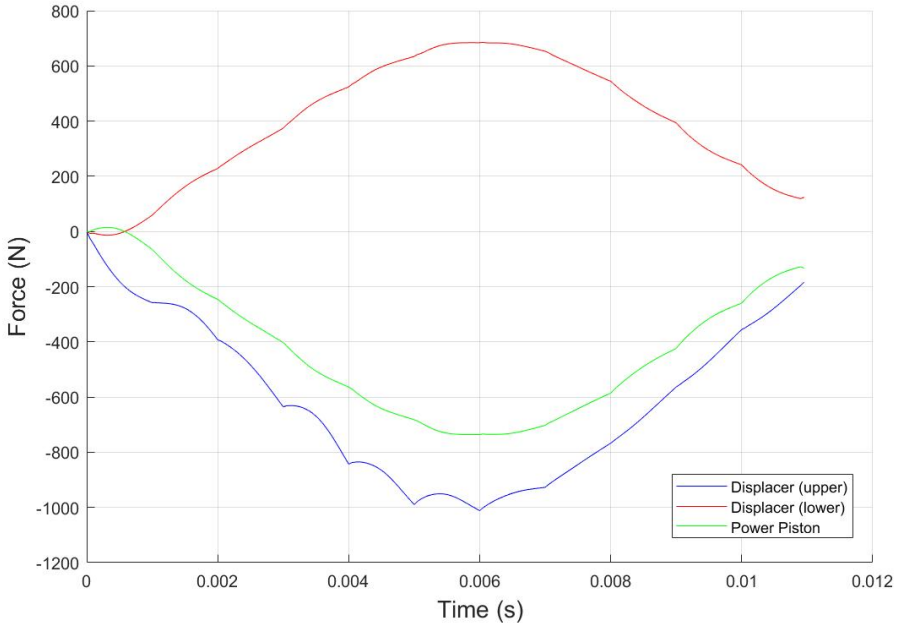

Figure 15. Plot of Piston Forces Over Time.

The results from this simulation were a step further toward model maturity for the methods used to characterize the Sunpower B-10 FPSE. The data gathered from a short simulation run time showed that the fluid and mesh moved in accordance with the principles identified in Schmidt Analysis. Furthermore, dynamic meshing and sizing techniques proved to be a successful method for modelling volume changes and for refining more intricate parts of the geometry, like the narrow channel.

Though the fluid was observed to carry heat between the expansion and compression spaces, the run time was not long enough to fully capture the effects of the thermal boundary conditions. As a result, there was not enough time for the heat to fully

diffuse through the working fluid, and the simulation and did not represent the steady state operating conditions of the FPSE.

Further tests must be conducted to fully characterize the behavior of the fluid. Once confidence is established in the model's operation, the data can be compared to experimental results for validation, and the method can be reapplied to the geometry and operating characteristics of the studied FPSEG.

IV. EXPERIMENTAL METHODS

Figures 16 and 17 show a full diagram and image of the FPSEG experimental setup, respectively. The heat source is an electric cooktop burner. Heat transfers directly from the burner through a thin-walled heat shield, and then to the heater head of the engine, raising the temperature of the working fluid in the expansion zone. To ensure consistency and properly record the energy input of the heat source, a variable transformer regulates the voltage input at a steady 120 V. Heat is continually added until the FPSEG reaches an appropriate starting temperature, which is 180°C for this particular device [33]. Next, water between 18°C and 20°C is circulated through the system to provide appropriate cooling to the cold compression zone. Circulation from the water reservoir to the FPSEG and back is achieved using an electric pump. Finally, sensor data and power output are recorded and displayed by the system controls box. Additional temperature data is gathered using the National Instruments PXIe-1082. This data acquisition will be explained in greater detail in section B.

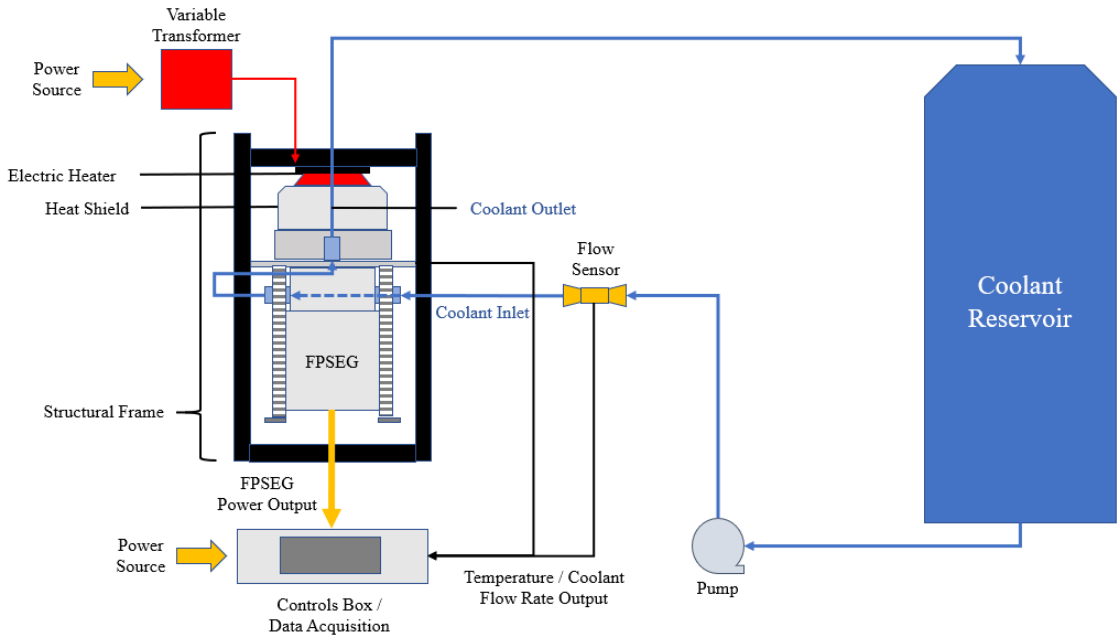

Figure 16. FPSEG Testing Apparatus and Setup Diagram.

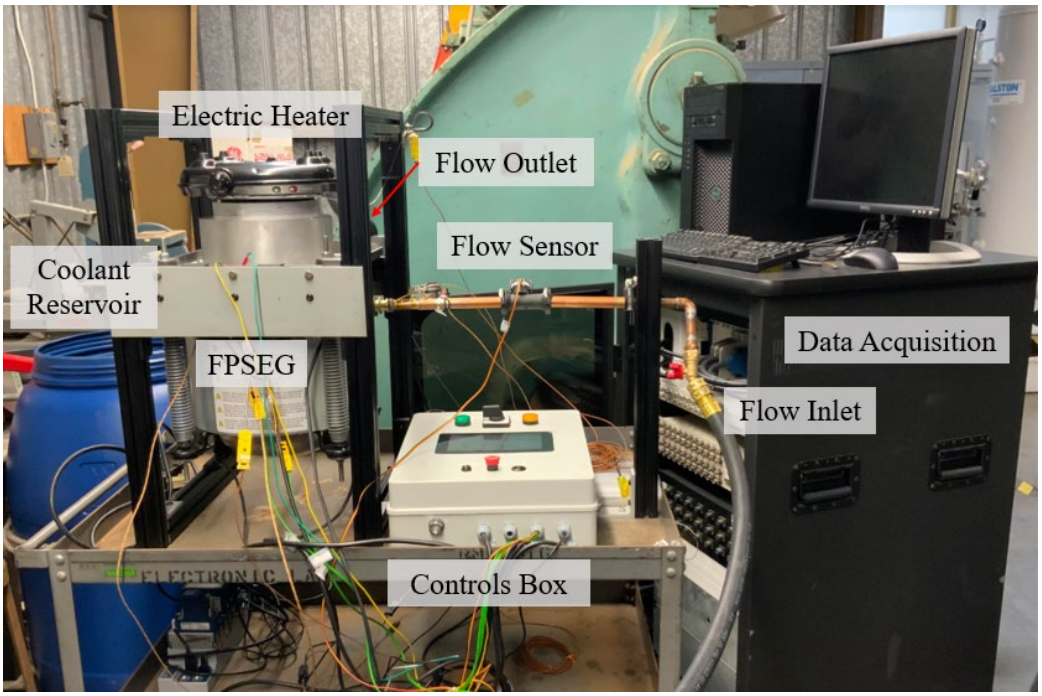

Figure 17. FPSEG Experimental Setup.

A. COMPONENT DESCRIPTION

1. Free-Piston Stirling Engine-Generator

The representative FPSEG investigated in this study is the Microgen Hanging Gas Engine, pictured in Figure 18. This particular FPSEG is designed to receive heat in the form of combusted natural gas and have an electrical power output of 1 kW. The working fluid is helium gas, which is charged to a pressure of 23 bar. As in the original Beale engine, the FPSEG of this study consists of a single cylinder assembly whereby the power piston and displacer piston are not mechanically linked, and piston phasing is completely dependent on gas dynamics. This greatly reduces frictional losses in operation. Additionally, a planar spring is connected to the power piston, which stores elastic potential energy with every downstroke, then pushes the piston back upward during the upstroke of the cycle. The expansion and compression zones are indicated in Figure 18 by the red and blue shaded spaces, respectively. The power piston is magnetic and coupled to a linear alternator – a fixed magnetic coil with copper windings. This allows the oscillatory motions

of the power piston to generate an alternating current, with a frequency related to that of the cycle. These FPSEGs are known to produce AC power between 50 and 60 Hz.

Benefits of the studied FPSEG include durability in rugged conditions, minimal maintenance with remote monitoring, quiet operation, a small footprint-ready to be integrated into existing systems, variation in heat sources, clean combustion and low emissions. The use of gas bearings between the pistons and cylinder reduces the friction at the sliding interfaces. Tightly produced parts, hermetically sealed, and natural frequencies also help them run indefinitely. As a result, it can theoretically run indefinitely with little to no maintenance [34]. Table 2 summarizes the FPSEG specifications.

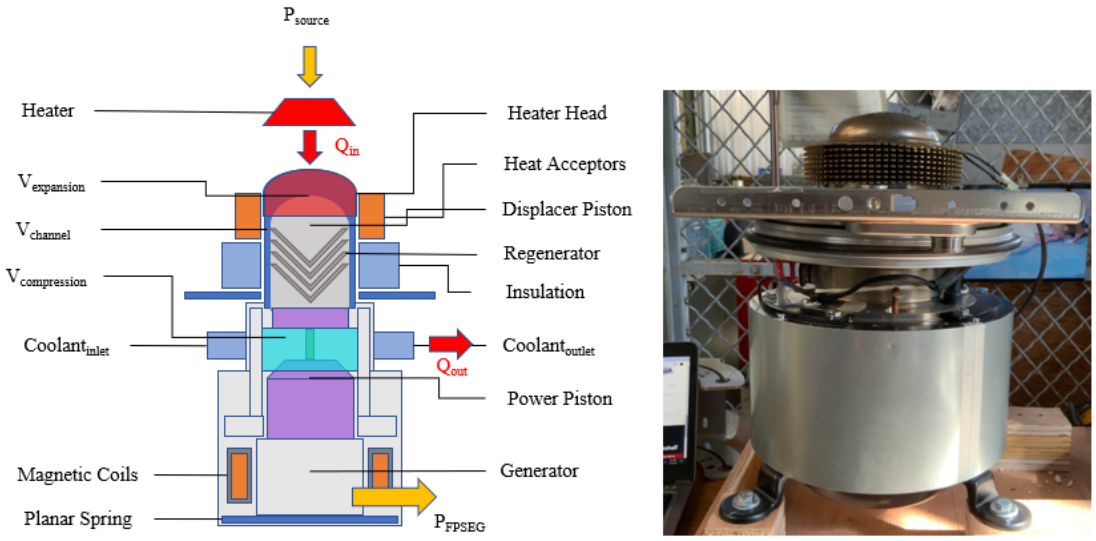

Figure 18. FPSEG Diagram (left) and Apparatus (right).

Table 2. FPSEG Specifications. Source: [34].

Specification	Values
Engine Mass	42 kg
Maximum Allowable Working Pressure (MAWP)	36.7 bar
Charge Pressure at 25°C	23 bar
Rated Output Power	1 KVA
Power Factor	> 0.95
Rated Voltage	230 Vrms
Rated Frequency	60 Hz
Noise at 1 meter	45 dB
Rated Engine Efficiency	26%
Design Life	50,000 hrs

2. Structural Frame

The structural frame was built to suspend the FPSEG such that all motion of the engine body, except vertical oscillations, was constrained. Figure 19 shows the engine frame design, which was built using aluminum railing. The railing was bolted to the steel plate, located below the heater head. It served as the primary hardpoint of the engine. Finally, the frame rigidly connects the hanging engine to a steel cart, while still providing room in suspension for the springs to freely absorb the vibrations. This assembly damps the engine motion, keeping it stable and quiet.

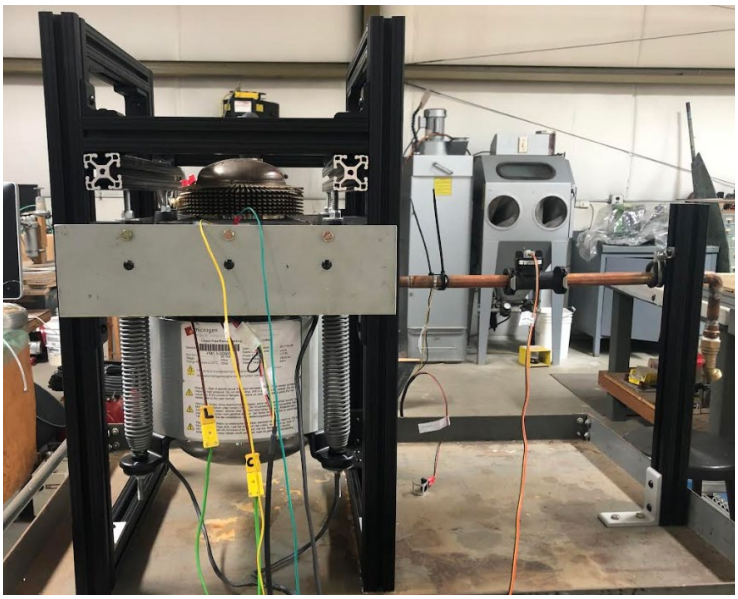

Figure 19. FPSEG Mounted to Aluminum Frame.

3. Springs and Damping

The engine has four damping springs, as shown in Figure 20. These attach to the central steel plate on the exterior of the engine and fasten to the base of the body. Using Hooke's Law, the spring constant for each spring was calculated to be 37.94 N·m.

Figure 20. Damping Springs.

4. Heating Unit

The heating unit used to supply thermal energy is a portable electric burner, typically used for cooking. The burner has a power rating of 1,100 W and can reach up to temperatures of 110°C. To control the power going into the burner, a variable transformer was used, which was set to an output of 120 V. This ensured that the burner was drawing a consistent amount of power for the duration of the engine runtime.

Figure 21. Electric Burner Heating Source.

5. Heat Shielding and Insulation

Because the electric burner supplies heat at a small rate to the engine, it was necessary to reduce losses between the burner and the engine heater head to allow the hot head temperature to rise continuously and reach the engine starting temperature. To resolve this, an aluminum heat shield was designed. The head of the shield, as shown in Figure 22, was 3D printed using the Xerox ElemX metal printer. This component was designed to conform to the dome-shaped heater head on the engine. The flat surface over the top allows for maximum surface contact between the electric burner and the shielding. A thickness of 2.54 mm at the top interface and 6.35 mm at the side face. This ensured that heat could conduct more freely between the heater and shield than through the sides of the shield wall and the environment. The cylindrical walls of the shield were made out of steel and had a wall thickness of 1.89 mm. A technical drawing of the dimensions of the 3D printed shield is recorded in Appendix E.

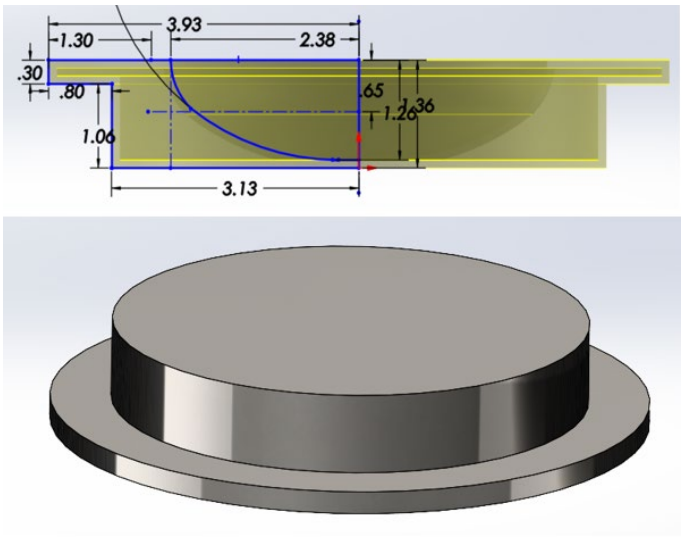

Figure 22. Heat Shield Top CAD Drawings Side Sketch (top) and Outside View (bottom).

Finally, fiberglass insulation was used to line the inside of the shield.

Figure 23. Heat Shield Insulation (left) and Assembly (right).

6. Coolant System

A series of hoses were used to circulate water from the reservoir, through the engine water jacket, and back. A 120 V electric power water pump was used to pump the water from the reservoir to the engine. The pump had a maximum flow rate of 1,249 L per hour

and a maximum lift of 11.88 m. Finally, the coolant reservoir was a rain barrel with a capacity to hold 208.19 gallons of fluid.

7. Controls Box

The engine controls box, as shown in Figure 24, is responsible for recording certain sensor data as well as reporting FPSEG power output and the overall operating conditions of the engine while in use. This includes coolant flow rates, internal temperatures, voltage input, current, engine frequency, runtime, error messages, as well as maintenance messages. The controls box received an electrical input of 220 V split phase power.

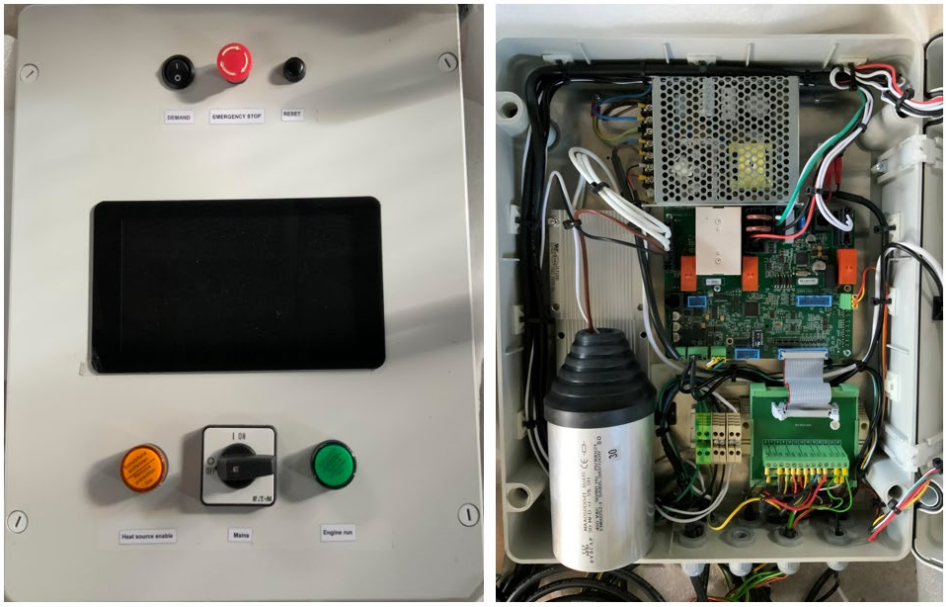

Figure 24. FPSEG Controls Box Exterior (left) and Interior (right).

B. DATA ACQUISITION

During engine operation, temperature data and coolant flow rate were recorded in order to construct an operating curve of the power output as the thermal conditions changed. The instrumentation used to record this data was the FPSEG's controls box and the National Instruments (NI) PXIe-1082.

Specific data displayed by the engine controls box is listed in Table 3. A video camera with a time stamp was used to record the monitor screen for each engine run.

Table 3. Controls Box Data Output.

Parameter	Description	Units
$T_{Head\ Control}$	Head Control Temperature	°C
ΔT_{Head}	Head Temperature Delta T	°C
$T_{Coolant\ Inlet}$	Coolant Inlet Temperature	°C
$T_{Coolant\ Outlet}$	Coolant Outlet Temperature	°C
T_{end}	Back End Temperature	°C
$T_{Ambient}$	Ambient Environment Temperature	°C
$\dot{V}_{coolant}$	Coolant Flow Rate	L/min
P_e	Electrical Power Output	W
V_{in}	Input Voltage	V
I_{Out}	Current Output	A
f	Operating Frequency	Hz
E	FPSEG Energy	kWh

1. Temperature Data

Separate from the FPSEG controls box, the National Instruments PXIe-1082 was used to write and record additional temperature data on the engine. Each of the temperatures displayed by the controls box was made redundant by connecting J type and K type thermocouples to the same locations as identified in Table 3. This provided a way to manipulate the data and evaluate the results. Having redundant temperature sensors between the controls box and external equipment also allowed for verification of sensor consistency. Table 4 summarizes the external temperature sensor equipment while Figure 25 shows where each thermocouple is located.

The determination of J type thermocouples versus K type thermocouples was based on availability as well as the expected temperature range of the measured object. K type thermocouples were used to record hot sections of the engine while J type thermocouples were used to record cooler sections of the engine.

Table 4. Temperature Sensors.

#	Parameter	Location	Thermocouple Type	Total Sensor Quantity	Instrumentation
1	$T_{Ambient}$	Environment	K	2	Controls Box and NI PXIe-1082
2	$T_{Coolant\ Inlet}$	Coolant temperature at the flow inlet	J	2	Controls Box and NI PXIe-1082
3	$T_{Coolant\ Outlet}$	Coolant temperature at the flow outlet	K	2	Controls Box and NI PXIe-1082
4	$T_{Heat\ Source}$	Temperature of the electric heater coil	K	1	NI PXIe-1082
5	$T_{Heater\ Head}$	Surface temperature of the engine heater head dome	K	1	NI PXIe-1082
6	$T_{Head\ Control}$	Surface temperature of the expansion side	J	2	Controls Box and NI PXIe-1082
7	$T_{Head\ Level}$	Surface temperature of the expansion side	K	2	Controls Box and NI PXIe-1082
8	$T_{Heat\ Shield}$	Temperature inside of the heat shield	K	1	NI PXIe-1082

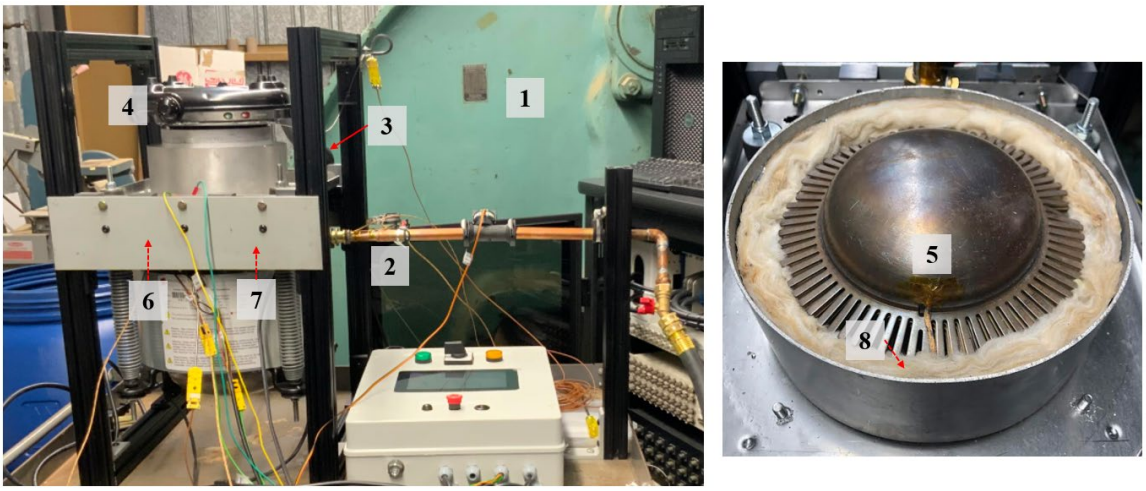

Figure 25. Thermocouple Locations.

2. Coolant Flow Rate

The Huba Control OEM Vortex Flow Sensor (Figure 26) was used to monitor and record the coolant flow rate through the FPSEG. It can read flow rates between 3.5 and 50 L/min.

Figure 26. Von Karman Vortex Sensor.

C. TESTING

Data for the FPSEG was recorded during three phases of the FPSEG operation: engine heating, engine startup, and engine shutdown. Four trials were conducted.

For each trial, the following steps were followed to achieve FPSEG operation: First, the electric heater was turned on to its maximum heating value, allowing the heater head to pre-heat until reaching a temperature of 100 °C. For higher energy heat sources with large rates of heat transfer, such as natural gas burners, this step is not necessary. Next, the coolant was set to flow at a rate between 8 and 10 L/min, as indicated by the controls box monitor. The temperature of the coolant at the inlet was not controlled, but varied between 18 °C and 19 °C. Next, the demand button was switched from zero to one, which enabled power from the generator to be grid-connected. In the case of this FPSEG, output power was read by the control box, then siphoned into a resistor to be burned off. The engine then enters Engine Control State 1, which indicates that the heater head is ready to receive heat. The heater is adjusted back to its maximum value until the engine reaches a sufficient heater head control temperature, which was 180 °C. Once these conditions are met, the engine's self-starting mechanisms activate and the FPSEG cycle begins. While in operation, the engine is in Engine Control State 5. Heat is continually added until one

minute after the engine starts. Then, the engine is allowed to run without a heat source until it shuts down.

Data collection began once the FPSEG reached a head temperature of 100 °C. The total duration of data collection for each trial was 905 seconds, where temperatures were recorded every 0.2 seconds.

V. RESULTS AND ANALYSIS

Six tests were conducted to observe the operation of the FPSEG. The first two trials were conducted using the electric burner as the heat source while the heat shield minimized thermal losses to the environment. Though the shield enabled the heater head to reach starting temperatures, the FPSEG did not start. As an alternate method of heating, the shield and insulation were removed, and an acetylene torch was used to distribute heat over the engine head. All other operating procedures remained constant. The starting conditions for each of the successful trials obtained from the controls box is summarized in Table 5.

Table 5. Engine Starting Conditions.

Trial	Head Control Temperature (°C)	Head Temperature Delta T (°C)	Coolant Inlet Temperature (°C)	Coolant Outlet Temperature (°C)
3	132	-83.0	17.4	16.0
4	163	-59.6	19.1	16.5
5	181	-40.4	20.5	16.5
6	192	-28.3	21	16.6

The head control temperature is the average internal temperature of the heater head gas, measured by two thermocouples. The head temperature delta T is the temperature difference between these two thermocouples. If the absolute value of the head temperature delta T became greater than 100 °C, the engine would not start. Thus, it was important to distribute the heat over the engine head as evenly as possible. Finally, coolant conditions were also observed. Though the starting temperature was expected to be 180 °C, these trials showed a range of 60 °C from the minimum observed starting temperature to the maximum. It is also shown that there appears to be a relationship between the head control temperature and the head temperature delta T. Lower starting temperatures corresponded to a larger head delta T. This could indicate that, due to uneven heating, the engine could prematurely

start if one of its internal thermocouples is reading a sufficiently high starting temperature. This was likely seen in Trial 3, which had the lowest observed starting temperature. Though heat was continuously applied to the engine head during this trial, the engine started and then shut down only nine seconds after the startup. The thermocouples read a high temperature, but there was not a sufficient amount of heat entering the engine head to maintain the Stirling cycle.

Trial 6, which was the most successful trial using these methods, is further evaluated. For this trial, the engine ran for a total of 87 seconds, with the heat source removed from the head after 60 seconds of run time. Data from the external temperature sensors for this test was extracted and compiled using MATLAB. Additional data from the controls box videos were recorded manually at a rate of one data point per second for each controls box parameter. The results obtained from each of these are plotted in Figures 27 through 30. The code used to plot this data is recorded in Appendix F.

Figure 27 shows a plot of the redundant temperature sensors, measured either by the NI PXIe-1082 or the controls box. These parameters included the head control temperature, coolant inlet temperature, and coolant outlet temperature. This data was plotted to view any discrepancies between the external data collecting system and the controls box sensors.

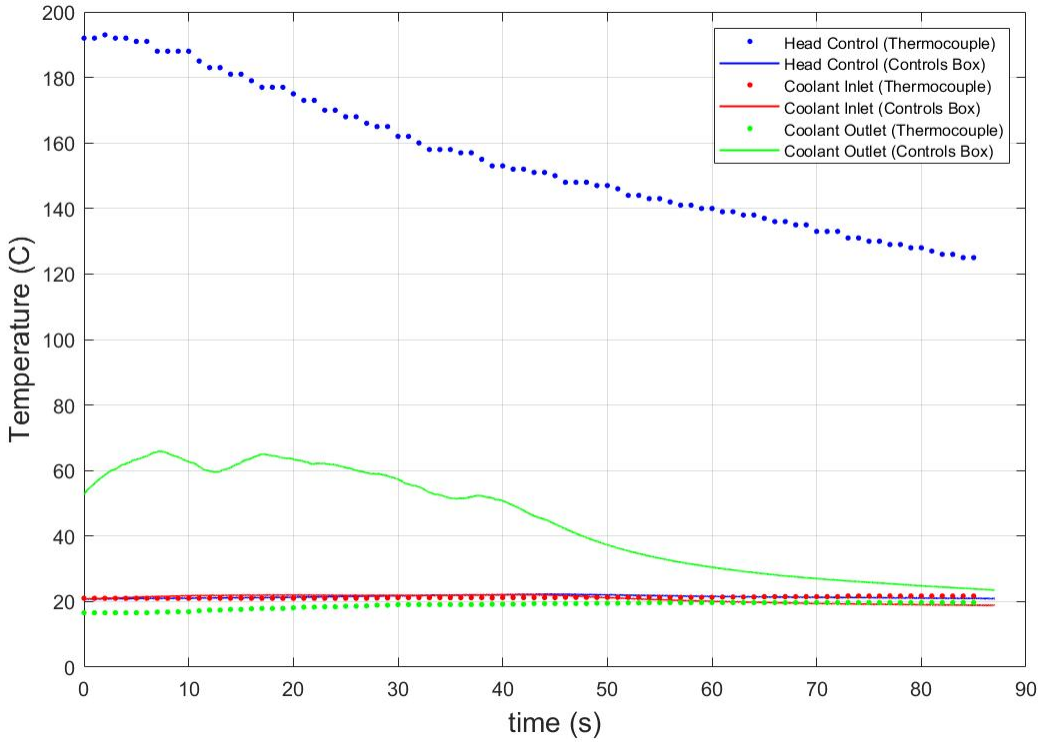

Figure 27. Redundant Temperatures Measured by External Thermocouples and the Controls Box.

This data begins when the engine starts and ends when the engine stops. The heating source was removed at the 60 second mark. Figure 27 shows that the greatest discrepancy between sensors is seen between the head control temperatures. Though the additional thermocouple was placed directly adjacent to where the engine's sensor was identified on the surface, this great disparity confirms that the engine's sensor is one that enters the engine internally, capturing data points that could not be physically reached by any surface thermocouple. Thus, the head control temperature recorded by the NI PXIe-1082 does not give the same information, and could not verify the controls box counterpart. The second disparity is shown between the coolant outlet temperatures. This is attributed to imperfect contact of the externally placed thermocouple to the surface of the outlet hose connection.

Figures 28 and 29 show the temperature data and electrical power output over time for the controls box sensors and the external sensors, respectively. For the external sensor data set, a fifteen second time frame was added to the front and back of the engine run time

to capture the pre and post-run moments. The red vertical lines on each figure indicate where the heat source was removed from the engine head.

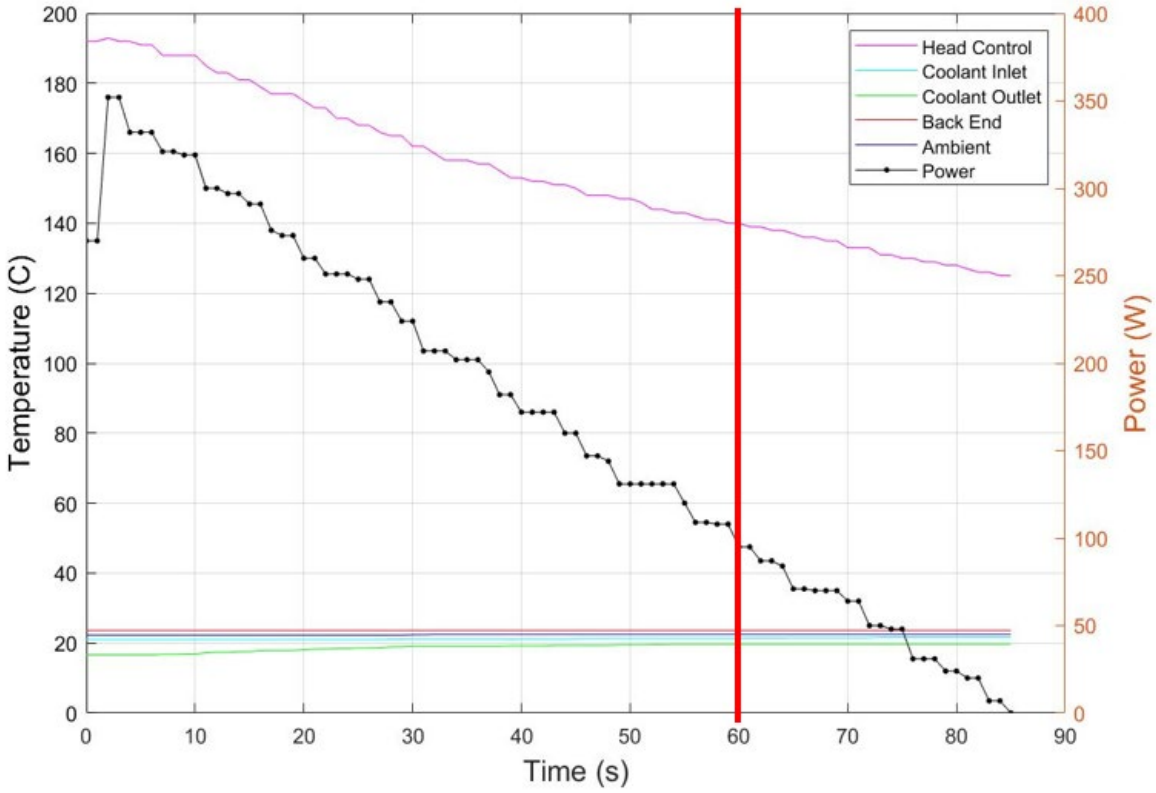

Figure 28. Controls Box Temperature Data.

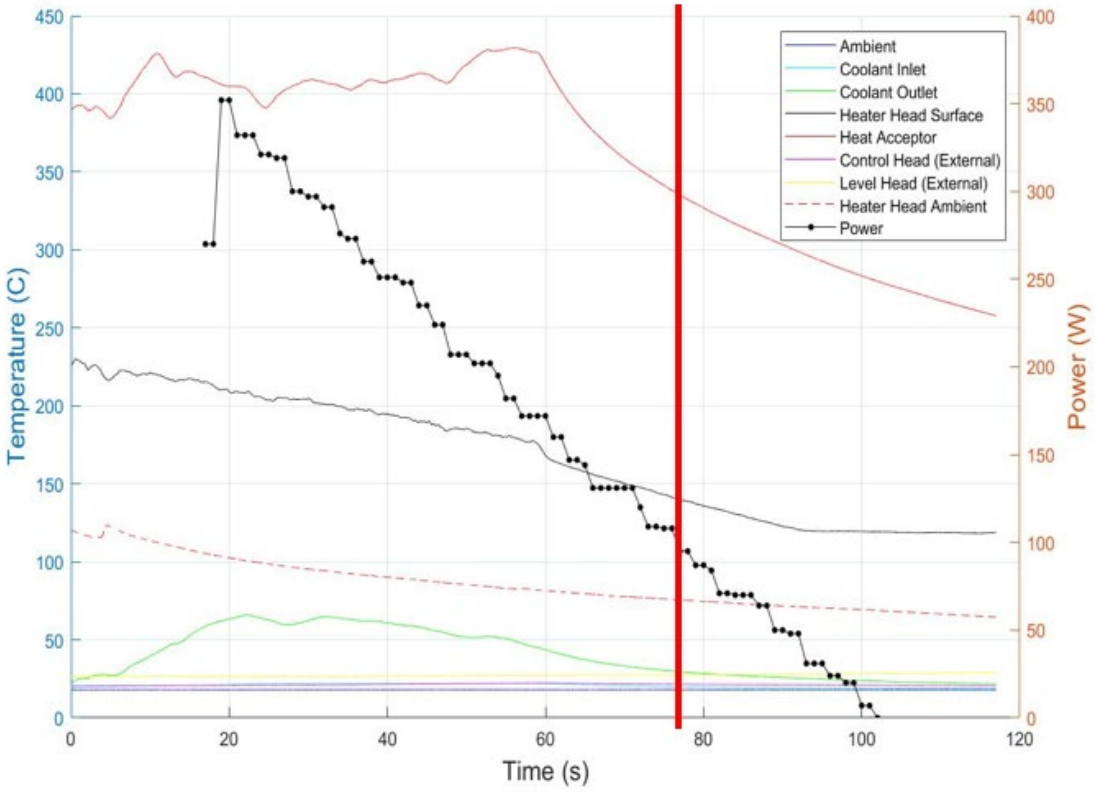

Figure 29. External Sensor Data.

For both Figures 28 and 29, it is shown that the power output and heater head temperatures are decreasing, even as heat is continually added to the system. This is inconsistent with the ideal Stirling cycle, which states that heating and cooling are isothermal during the expansion and compression processes. This cycle is not ideal, which means that this trend could be attributed to multiple sources: First, because the run time is very short—only 87 seconds in total—it is expected that the power output of the engine has not stabilized and is in a transient state. The heat source is removed before stabilization is reached, and the data set is likely only capturing the start of the engine run. If allowed to reach steady state, the power output would increase with increasing heater head temperature, while the coolant temperature is constant. Second, it is possible that after the engine starts, the heat transfer going into the engine is less than what is required to maintain consistent operation. Prior to the engine start, all energy entering the heater head contributed to a rise in the working fluid temperature. However, once the engine started

and the pistons began to oscillate, the energy entering the heater head was used up more quickly than it was being supplied. As a result, a net decrease in heater head temperature was observed. Third, the trend is also an effect of uneven heating. Though the temperature sensors indicate that sufficient thermal energy has been supplied, this could also be skewed as the blow torch provided uneven heating to the system, by nature of its concentrated distribution. As a result, the location of the heater head thermocouple could be reading higher than the average temperature of the expansion side gas in moments when the torch was directly above this temperature sensor. Fourth, instability could be an effect of running the engine close to its minimum temperature. Multiple studies show that a FPSEGs thermal-to-electric efficiency increases at higher operating temperatures.

Finally, Figure 30 shows the relationship found between the power output of the engine and the heat source and sink temperature difference. T_H and T_C are the head control temperature and coolant inlet temperature, respectively, as recorded through the controls box. The plot shows a positive correlation between the electrical power output and the engine temperature difference. The data appears to be linear, as expected. Because this data is preliminary and the curve is only representative of the engine start, a regression is not characterized with this data to predict engine power output for increasing temperature differences.

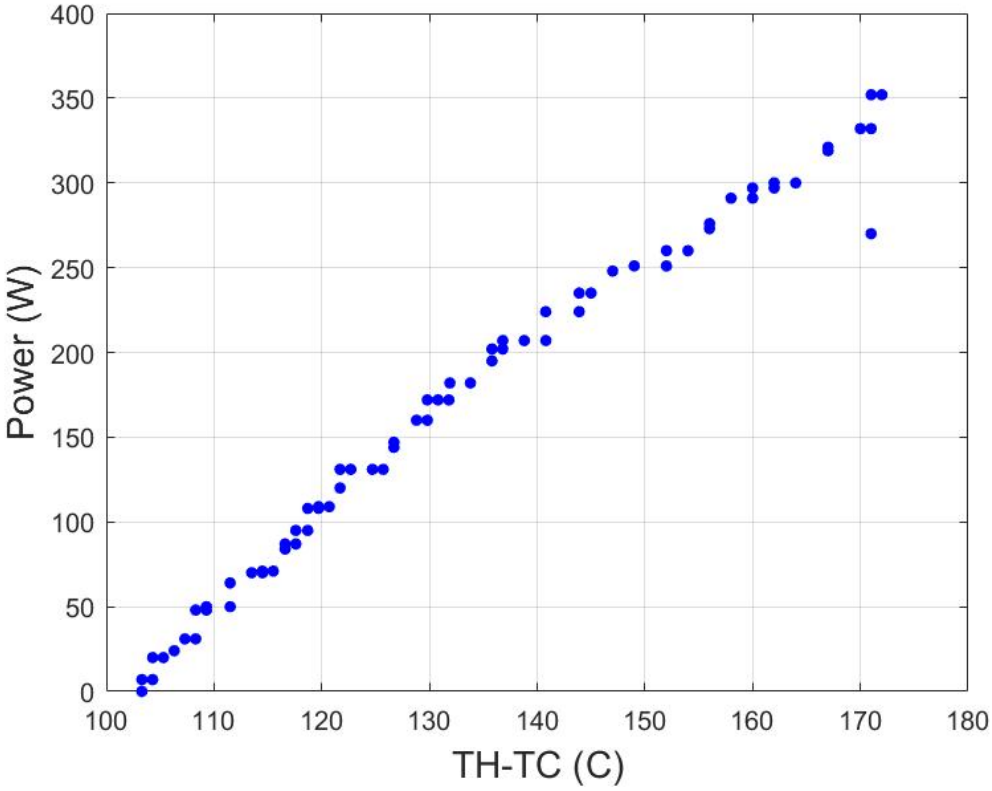

Figure 30. Plot of Engine Output Power Versus Temperature Difference.

THIS PAGE INTENTIONALLY LEFT BLANK

VI. CONCLUSION AND FUTURE WORK

A. CONCLUSION

This thesis investigated the operation of a FPSEG. A full testing apparatus was constructed to include the FPSEG framework, coolant system, and heating unit assembly. Starting conditions and operating procedures were identified and tested. Demonstration of the fully operating system was achieved, though alternative heating methods were used. Over the four engine runs conducted, it was shown that the PRSEG is capable of operating at low temperatures, with the lowest achieved startup observed at 130 °C. The maximum observed run for this engine was 87 seconds long, operated at a starting temperature of 192 °C, and produced a maximum power output of 352 W. Because the engine run time was short, and the data was most likely reflective of transient conditions, the operating curve obtained from this experiment is a preliminary result that was not extrapolated.

In tandem with the FPSEG experimental testing, development of a CFD model of the system progressed. Though piston motion was achieved and thermal communication was observed, consistent with the assumptions of Schmidt Analysis, the simulation must be tested further to fully validate the modelling method. As a result, further efforts are necessary to improve this model and later construct a model for the studied FPSEG in this thesis.

B. FUTURE WORK AND RECOMMENDATIONS

1. Improving the Heat Source

A high temperature heating source, capable of reaching temperatures of at least 200 °C, that can quickly and evenly distribute heat to the engine head should be integrated into the testing apparatus. It was found that evenly heating the engine head is a significant factor that affects the sustained operation of the engine after startup. Efforts should be made in designing a heat source that can be controlled by the user to maintain or adjust the header head temperature while in operation. One possible option could include wrapping an induction coil around the heater head and controlling the power input with a variable

transformer. Furthermore, efforts to calculate the heat transferred from the source to the engine should be made so that the thermal to electric efficiency can be calculated.

2. Extended Testing

Further tests should be conducted to increase the fidelity of the data. It would be useful to run multiple engine tests for longer periods and a wider range of heater head temperatures. For a constant heater head temperature, each test should run until the observed power output levels out and becomes constant. This should be repeated for temperatures between 150 °C and 500 °C, at intervals of 25 °C. These temperatures are representative of other systems that the studied FPSEG could potentially be coupled with in the future. In the interest of waste heat recovery, low-grade waste heat is defined as temperatures lower than 100 °C, medium-grade waste heat is defined as temperatures between 100 °C and 400 °C, and high-grade waste heat is defined as temperatures greater than 400 °C. Furthermore, solar systems are known to produce temperatures as high as 300 °C. With data capturing the steady state power output at many heater head temperatures, a more refined operating curve can be constructed to which a correlation can be made to then predict the engine's power output for other conditions. By conducting these tests, the engine's ability to recover heat from waste heat, solar systems, and other heat sources can be better understood.

3. LAES Integration

In the interest of LAES system coupling, a test using liquid air as the coolant fluid should be conducted to observe any significance in engine operation. It is suspected, based on these preliminary experiments, that the engine controls box will not start the FPSEG unless it identifies through its thermocouples that the heater head has reached a sufficiently high starting temperature. As a result, using liquid air alone to create a temperature difference with the ambient air—though in theory would induce the Stirling cycle—may not satisfy the starting conditions of the studied FPSEG. Thus, this test should be conducted using both liquid air coolant and a heating source over the engine head. The temperature difference caused by the cryogenic T_C should result in a dramatic increase in power output

compared to the results using water. Increasing the heater head temperature should further magnify this effect.

If the engine can operate with a cryogenic cooling system, further efforts should be made to fully integrate the studied FPSEG as part of the LAES recovery system and microgrid. A potential system, adapted from Howe et al. [34], would look like Figure 31, whereby air is liquified using excess generated energy on the compression side, and electrical power is generated from the temperature difference on the FPSEG side.

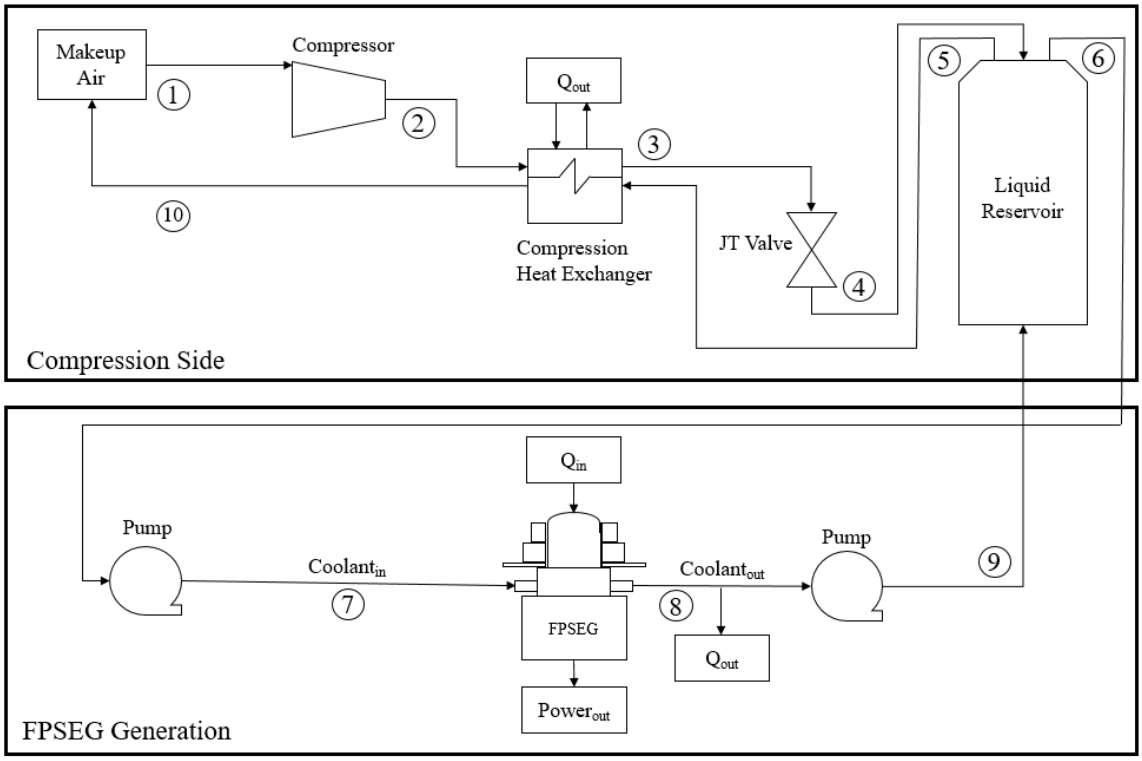

Figure 31. Component Diagram of LAES and FPSEG Combined System.

4. ANSYS Fluent Model

Finally, efforts to continue testing the Sunpower B-10 model, and eventually finish the model of the studied FPSEG should be made. Once the method is validated for the Sunpower B-10, it should be applied to the geometry of the studied FPSEG, as shown in Figure 32. Because these geometric parameters are not available, estimations were made

based off of external measurements taken of the engine. The channel thickness was assumed to be the same as that of the Sunpower B-10.

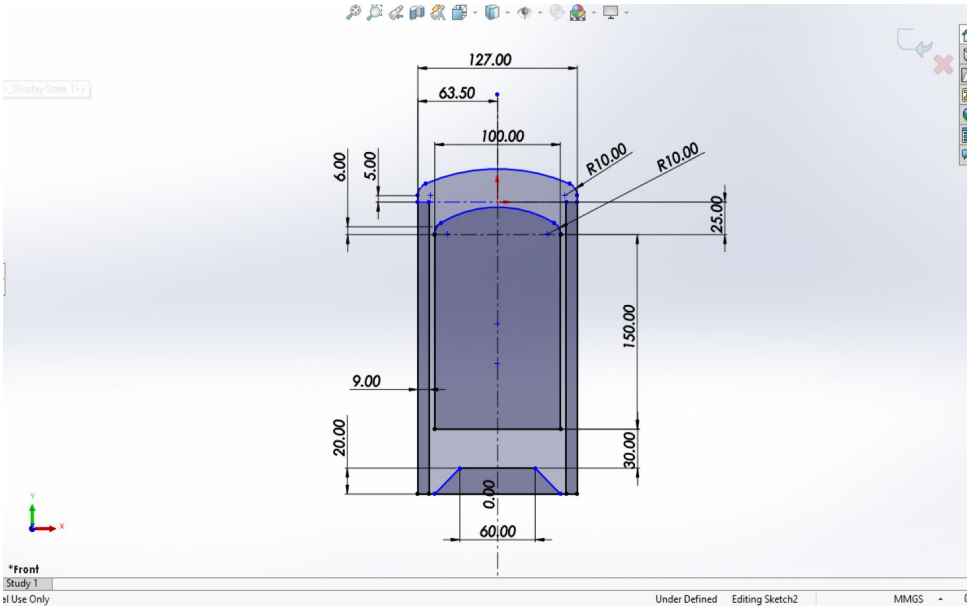

Figure 32. FPSEG Estimated Model Geometry.

APPENDIX A. MATLAB CODE FOR PISTON MOTION PROFILES

Appendix A shows the MATLAB code that was developed to generate the motion profiles for the displacer and power pistons. This code is based off assumptions from Schmidt cycle analysis, which means that piston motion is simplified to sinusoidal motion with a defined phase difference between them. Parameters input into this code derives from the references listed in the code.

```
% Schmidt Analysis Piston Motion UDF
% References:
% [1] Mou et al., "A Numerical Model on
Thermodynamic Analysis of Free Piston
% Stirling Engines"
% [2] Ridha et al., "Two-dimensional CFD
simulation coupled with 6DOF solver for
% analyzing operating process of free piston
stirling engine"
% [3] Saturno, "Some Mathematical Models to
Describe the Dynamic Behavior
% of the B-10 Free-Piston Stirling Engine"

clear all, close all, clc

% Engine Parameters
Ap = 1.01e-3; % [m^2] cross sectional area
power piston
Ad = 9.0792e-4; % [m^2] cross sectional area
displacer piston
Ar = 1.26677e-4; %[m^2] cross sectional area
rod
mp = 0.5295; % [kg] mass power piston
md = 0.0867; % [kg] mass displacer piston
Vh = 8.567e-6; % [m^3] volume hot expansion
side @ equilibrium
Vc = 16.036e-6; % [m^3] volume cold compression
side @ equilibrium
```

```
frequency = 60; % [Hz] ** Not sure about this
value, using nominal f for now
PAmplitude = 0.0053; % [m]
DAmplitude = 0.0064; % [m]
theta = 58.81*pi/180; % [rad/s] phase
difference between pistons
omega = 2*pi*frequency; %[rad/s] engine angular
speed
T = 1/frequency; % Period

% Movement UDF based on Ref. 1
displacer_motion = @(t)
DAmplitude*sin(omega.*t);
power_motion = @(t) PAmplitude*sin(omega.*t-
theta);

time  = [0:0.001:12*T]'; % [s] period must be
in multipled of 6 for 0.1 sec of run time
y_displacer = displacer_motion(time);
y_power = power_motion(time);

figure (1)
plot(time,y_displacer)
hold on
plot(time,y_power)
legend('displacer','power')
xlabel('time (s)')
ylabel('y (m)')
```

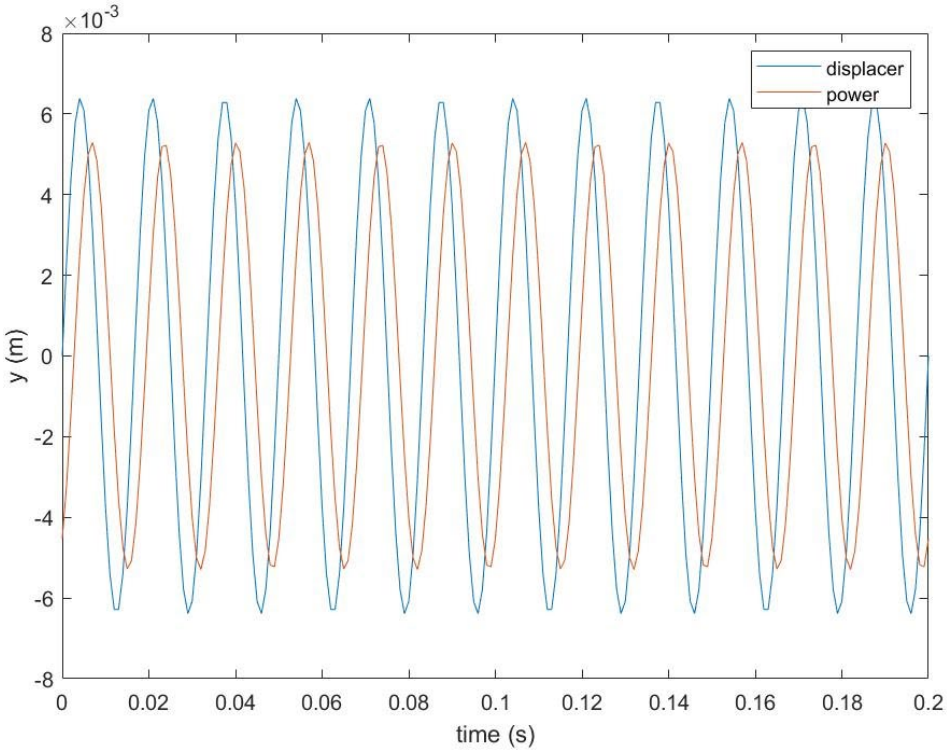
×10^-3
8
6
4
2
0
-2
-4
-6
-8
y (m)
0
0.02
0.04
0.06
0.08
0.1
0.12
0.14
0.16
0.18
0.2
time (s)
displacer
power

THIS PAGE INTENTIONALLY LEFT BLANK

APPENDIX B. PISTON MOTION PROFILES

Appendix B shows the resulting piston motion profiles that were generated from the MATLAB code in Appendix A. These profiles were read into the ANSYS Fluent simulation as a .prof file.

Displacer Piston Profile:
displacerprofile 2 201 0
time y

0	0.000000
0.001	0.002356
0.002	0.004381
0.003	0.005791
0.004	0.006387
0.005	0.006087
0.006	0.004931
0.007	0.003083
0.008	0.000802
0.009	-0.001592
0.01	-0.003762
0.011	-0.005404
0.012	-0.006287
0.013	-0.006287
0.014	-0.005404
0.015	-0.003762
0.016	-0.001592
0.017	0.000802
0.018	0.003083
0.019	0.004931
0.02	0.006087
0.021	0.006387
0.022	0.005791
0.023	0.004381
0.024	0.002356
0.025	0.000000
0.026	-0.002356
0.027	-0.004381
0.028	-0.005791
0.029	-0.006387
0.03	-0.006087
0.031	-0.004931
0.032	-0.003083

0.033 -0.000802
0.034 0.001592
0.035 0.003762
0.036 0.005404
0.037 0.006287
0.038 0.006287
0.039 0.005404
0.04 0.003762
0.041 0.001592
0.042 -0.000802
0.043 -0.003083
0.044 -0.004931
0.045 -0.006087
0.046 -0.006387
0.047 -0.005791
0.048 -0.004381
0.049 -0.002356
0.05 0.000000
0.051 0.002356
0.052 0.004381
0.053 0.005791
0.054 0.006387
0.055 0.006087
0.056 0.004931
0.057 0.003083
0.058 0.000802
0.059 -0.001592
0.06 -0.003762
0.061 -0.005404
0.062 -0.006287
0.063 -0.006287
0.064 -0.005404
0.065 -0.003762
0.066 -0.001592
0.067 0.000802
0.068 0.003083
0.069 0.004931
0.07 0.006087
0.071 0.006387
0.072 0.005791
0.073 0.004381
0.074 0.002356
0.075 0.000000
0.076 -0.002356
0.077 -0.004381

0.078 -0.005791
0.079 -0.006387
0.08 -0.006087
0.081 -0.004931
0.082 -0.003083
0.083 -0.000802
0.084 0.001592
0.085 0.003762
0.086 0.005404
0.087 0.006287
0.088 0.006287
0.089 0.005404
0.09 0.003762
0.091 0.001592
0.092 -0.000802
0.093 -0.003083
0.094 -0.004931
0.095 -0.006087
0.096 -0.006387
0.097 -0.005791
0.098 -0.004381
0.099 -0.002356
0.1 0.000000
0.101 0.002356
0.102 0.004381
0.103 0.005791
0.104 0.006387
0.105 0.006087
0.106 0.004931
0.107 0.003083
0.108 0.000802
0.109 -0.001592
0.11 -0.003762
0.111 -0.005404
0.112 -0.006287
0.113 -0.006287
0.114 -0.005404
0.115 -0.003762
0.116 -0.001592
0.117 0.000802
0.118 0.003083
0.119 0.004931
0.12 0.006087
0.121 0.006387
0.122 0.005791

0.123 0.004381
0.124 0.002356
0.125 0.000000
0.126 -0.002356
0.127 -0.004381
0.128 -0.005791
0.129 -0.006387
0.13 -0.006087
0.131 -0.004931
0.132 -0.003083
0.133 -0.000802
0.134 0.001592
0.135 0.003762
0.136 0.005404
0.137 0.006287
0.138 0.006287
0.139 0.005404
0.14 0.003762
0.141 0.001592
0.142 -0.000802
0.143 -0.003083
0.144 -0.004931
0.145 -0.006087
0.146 -0.006387
0.147 -0.005791
0.148 -0.004381
0.149 -0.002356
0.15 0.000000
0.151 0.002356
0.152 0.004381
0.153 0.005791
0.154 0.006387
0.155 0.006087
0.156 0.004931
0.157 0.003083
0.158 0.000802
0.159 -0.001592
0.16 -0.003762
0.161 -0.005404
0.162 -0.006287
0.163 -0.006287
0.164 -0.005404
0.165 -0.003762
0.166 -0.001592
0.167 0.000802

0.168 0.003083
0.169 0.004931
0.17 0.006087
0.171 0.006387
0.172 0.005791
0.173 0.004381
0.174 0.002356
0.175 0.000000
0.176 -0.002356
0.177 -0.004381
0.178 -0.005791
0.179 -0.006387
0.18 -0.006087
0.181 -0.004931
0.182 -0.003083
0.183 -0.000802
0.184 0.001592
0.185 0.003762
0.186 0.005404
0.187 0.006287
0.188 0.006287
0.189 0.005404
0.19 0.003762
0.191 0.001592
0.192 -0.000802
0.193 -0.003083
0.194 -0.004931
0.195 -0.006087
0.196 -0.006387
0.197 -0.005791
0.198 -0.004381
0.199 -0.002356
0.2 0.000000

Power Piston Profile:
powerprofile 2 201 0
time y
0 -0.004534
0.001 -0.003205
0.002 -0.001426
0.003 0.000553
0.004 0.002455
0.005 0.004011
0.006 0.005005
0.007 0.005295

0.008 0.004842
0.009 0.003709
0.01 0.002055
0.011 0.000112
0.012 -0.001847
0.013 -0.003546
0.014 -0.004747
0.015 -0.005281
0.016 -0.005074
0.017 -0.004154
0.018 -0.002651
0.019 -0.000775
0.02 0.001209
0.021 0.003024
0.022 0.004414
0.023 0.005184
0.024 0.005226
0.025 0.004534
0.026 0.003205
0.027 0.001426
0.028 -0.000553
0.029 -0.002455
0.03 -0.004011
0.031 -0.005005
0.032 -0.005295
0.033 -0.004842
0.034 -0.003709
0.035 -0.002055
0.036 -0.000112
0.037 0.001847
0.038 0.003546
0.039 0.004747
0.04 0.005281
0.041 0.005074
0.042 0.004154
0.043 0.002651
0.044 0.000775
0.045 -0.001209
0.046 -0.003024
0.047 -0.004414
0.048 -0.005184
0.049 -0.005226
0.05 -0.004534
0.051 -0.003205
0.052 -0.001426

0.053 0.000553
0.054 0.002455
0.055 0.004011
0.056 0.005005
0.057 0.005295
0.058 0.004842
0.059 0.003709
0.06 0.002055
0.061 0.000112
0.062 -0.001847
0.063 -0.003546
0.064 -0.004747
0.065 -0.005281
0.066 -0.005074
0.067 -0.004154
0.068 -0.002651
0.069 -0.000775
0.07 0.001209
0.071 0.003024
0.072 0.004414
0.073 0.005184
0.074 0.005226
0.075 0.004534
0.076 0.003205
0.077 0.001426
0.078 -0.000553
0.079 -0.002455
0.08 -0.004011
0.081 -0.005005
0.082 -0.005295
0.083 -0.004842
0.084 -0.003709
0.085 -0.002055
0.086 -0.000112
0.087 0.001847
0.088 0.003546
0.089 0.004747
0.09 0.005281
0.091 0.005074
0.092 0.004154
0.093 0.002651
0.094 0.000775
0.095 -0.001209
0.096 -0.003024
0.097 -0.004414

0.098 -0.005184
0.099 -0.005226
0.1 -0.004534
0.101 -0.003205
0.102 -0.001426
0.103 0.000553
0.104 0.002455
0.105 0.004011
0.106 0.005005
0.107 0.005295
0.108 0.004842
0.109 0.003709
0.11 0.002055
0.111 0.000112
0.112 -0.001847
0.113 -0.003546
0.114 -0.004747
0.115 -0.005281
0.116 -0.005074
0.117 -0.004154
0.118 -0.002651
0.119 -0.000775
0.12 0.001209
0.121 0.003024
0.122 0.004414
0.123 0.005184
0.124 0.005226
0.125 0.004534
0.126 0.003205
0.127 0.001426
0.128 -0.000553
0.129 -0.002455
0.13 -0.004011
0.131 -0.005005
0.132 -0.005295
0.133 -0.004842
0.134 -0.003709
0.135 -0.002055
0.136 -0.000112
0.137 0.001847
0.138 0.003546
0.139 0.004747
0.14 0.005281
0.141 0.005074
0.142 0.004154

0.143 0.002651
0.144 0.000775
0.145 -0.001209
0.146 -0.003024
0.147 -0.004414
0.148 -0.005184
0.149 -0.005226
0.15 -0.004534
0.151 -0.003205
0.152 -0.001426
0.153 0.000553
0.154 0.002455
0.155 0.004011
0.156 0.005005
0.157 0.005295
0.158 0.004842
0.159 0.003709
0.16 0.002055
0.161 0.000112
0.162 -0.001847
0.163 -0.003546
0.164 -0.004747
0.165 -0.005281
0.166 -0.005074
0.167 -0.004154
0.168 -0.002651
0.169 -0.000775
0.17 0.001209
0.171 0.003024
0.172 0.004414
0.173 0.005184
0.174 0.005226
0.175 0.004534
0.176 0.003205
0.177 0.001426
0.178 -0.000553
0.179 -0.002455
0.18 -0.004011
0.181 -0.005005
0.182 -0.005295
0.183 -0.004842
0.184 -0.003709
0.185 -0.002055
0.186 -0.000112
0.187 0.001847

0.188	0.003546
0.189	0.004747
0.19	0.005281
0.191	0.005074
0.192	0.004154
0.193	0.002651
0.194	0.000775
0.195	-0.001209
0.196	-0.003024
0.197	-0.004414
0.198	-0.005184
0.199	-0.005226
0.2	-0.004534

APPENDIX C. ANSYS FLUENT SETTINGS

Appendix C is the report generated from the ANSYS Fluent simulation and describes the settings used to construct the model. The file report lists the date the report is generated and the location of the saved files. The mesh report lists the mesh information for each of the created model domains. The domains for this geometry are defined as the channel, compression zone, and expansion zone. Information about the number of nodes and cell shapes are shown for each domain. The physics report shows the boundary conditions defined for the edges in each domain. Finally, the picture report shows a wireframe of the geometry.

1. File Report

Table 1. File Information for FFF

Case	FFF
File Path	C:\Users\sarah.nguyen\OneDrive - Naval Postgraduate School\Desktop\Sunpower_6_1_files\dp0\FFF\Fluent\FFF.1-1-00220.dat.gz
File Date	02 June 2022
File Time	01:32:54 PM
File Type	FLUENT
File Version	19.2.0

2. Mesh Report

Table 2. Mesh Information for FFF

Domain	Nodes	Elements	Tetrahedra	Wedges	Pyramids	Hexahedra	Polyhedra
channel	16780	7881	0	1	0	7880	0
compression zone	1016	854	0	854	0	0	0
expansion zone	1102	991	0	991	0	0	0
All Domains	18898	9726	0	1846	0	7880	0

Table 3. Mesh Statistics for FFF

Domain	Minimum Face Angle	Maximum Face Angle	Maximum Edge Length Ratio	Maximum Element Volume Ratio	Connectivity Range	
channel	58.9888 [degree]	113.121 [degree]	33.9086	128.51	1	5
compression zone	5.53038 [degree]	139.252 [degree]	163.54	58.1912	1	11
expansion zone	20.6075 [degree]	122.676 [degree]	219.805	5.62877	1	9
All Domains	5.53038 [degree]	139.252 [degree]	219.805	128.51	1	11

3. Physics Report

Table 4. Domain Physics for FFF

Domain - channel	
Type	cell
Domain - compression zone	
Type	cell
Domain - expansion zone	
Type	cell

Table 5. Boundary Physics for FFF

Domain	Boundaries	
channel	**Boundary - ch to comp horizontal 2**	
	Type	INTERFACE
	Boundary - ch to ex horizontal 1	
	Type	INTERFACE
	Boundary - channel symmetry 1	
	Type	SYMMETRY
	Boundary - channel symmetry 2	
	Type	SYMMETRY
	Boundary - cylinder wall channel	
	Type	WALL
	Boundary - displacer piston channel	
	Type	WALL
compression zone	**Boundary - ch to comp horizontal 1**	
	Type	INTERFACE
	Boundary - comp to int vertical 1	
	Type	INTERFACE
	Boundary - comp to int vertical 2	
	Type	INTERFACE
	Boundary - compression zone symmetry 1	
	Type	SYMMETRY
	Boundary - compression zone symmetry 2	
	Type	SYMMETRY
	Boundary - cylinder wall compression zone	
	Type	WALL
	Boundary - displacer piston compression zone	
	Type	WALL
	Boundary - power piston	
	Type	WALL
	Boundary - rod wall	
	Type	WALL
expansion zone	**Boundary - ch to ex horizontal 2**	
	Type	INTERFACE
	Boundary - cylinder wall expansion zone	
	Type	WALL
	Boundary - displacer piston expansion zone	
	Type	WALL
	Boundary - ex to int vertical 1	
	Type	INTERFACE
	Boundary - ex to int vertical 2	
	Type	INTERFACE
	Boundary - expansion zone symmetry 1	
	Type	SYMMETRY
	Boundary - expansion zone symmetry 2	
	Type	SYMMETRY
	Boundary - hot source	
	Type	WALL
	Boundary - sym	
	Type	SYMMETRY

4. Pictures

Figure 1. Iso View of Wireframe

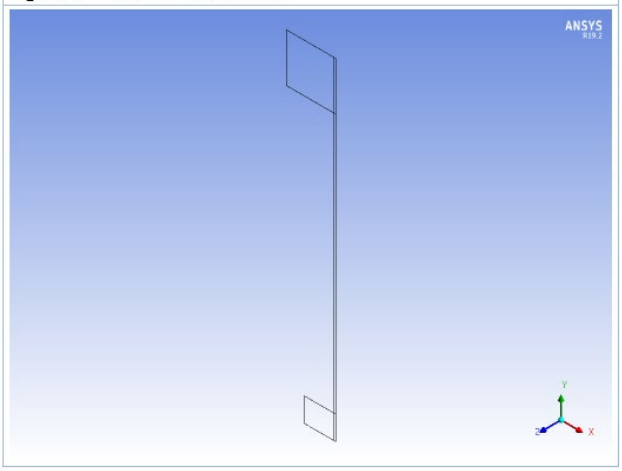

THIS PAGE INTENTIONALLY LEFT BLANK

APPENDIX D. MATLAB CODE FOR ANSYS FLUENT PLOTS

Appendix D shows the MATLAB code that was used to plot the data from the ANSYS Fluent simulations. Data from ANSYS Fluent was imported into MATLAB as "Data1.out." All of the resulting plots are shown after the code.

```
% Fluent Plots
clear all, close all, clc

Data = importfile('Data1.out');

time = Data{:,2};

P_total   = Data{:,12};      % [Pa] Avg
pressure of total volume
P_comp    = Data{:,7};       % [Pa] Avg
pressure of compression space
P_exp     = Data{:,8};       % [Pa] Avg
pressure of expansion space
P_channel = Data{:,6};       % [Pa] Avg
pressure of channel

T_total   = Data{:,13};      % [K] Avg
temperature of total volume
T_comp    = Data{:,10};      % [K] Avg
temperature of compression space
T_exp     = Data{:,11};      % [K] Avg
temperature of expansion space
T_channel = Data{:,9};       % [K] Avg
temperature of channel

V_total   = Data{:,16};      % [m^3] Volume
total
V_comp    = Data{:,14};      % [m^3] Volume
compression space
```

```
V_exp      = Data{:,15};       % [m^3] Volume
expansion space

F_displacer_upper = Data{:,18}; % [N] Avg force
over the surface of the top of the displacer
F_displacer_lower = Data{:,17}; % [N] Avg force
over the surface of the bottom of the displacer
F_powerpiston     = Data{:,19}; % [N] Avg force
over the surface of the top of the power piston

v_check1 = Data{:,21}; % [m/s] Avg y-velocity
at the boundary between the expansion space and
the channel
v_check2 = Data{:,20};  % [m/s] Avg y-velocity
at the boundary between the compression space
and the channel

% Pressures v. Time Plot
figure (1)
hold on
plot(time,P_total,'-b','markersize',25);
plot(time,P_exp,'-r','markersize',25);
plot(time,P_comp,'-g','markersize',25);
plot(time,P_channel,'-m','markersize',25);
ylabel('Pressure (Pa)',"Fontsize",14)
xlabel('Time (s)',"Fontsize", 14)
legend('Total Pressure','Expansion
Space','Compression Space','Channel')
grid on
hold off

% Temperatures v. Time Plot
figure (2)
hold on
plot(time,T_total,'-b','markersize',25);
plot(time,T_exp,'-r','markersize',25);
plot(time,T_comp,'-g','markersize',25);
plot(time,T_channel,'-m','markersize',25);
```

```
ylabel('Temperature (K)',"Fontsize",14)
xlabel('Time (s)',"Fontsize", 14)
legend('Total Temperature','Expansion
Space','Compression Space','Channel')
grid on
hold off

% Volumes v. Time Plot
figure (3)
hold on
plot(time,V_total,'-b','markersize',25);
plot(time,V_exp,'-r','markersize',25);
plot(time,V_comp,'-g','markersize',25);
ylabel('Volume (m^3)',"Fontsize",14)
xlabel('Time (s)',"Fontsize", 14)
legend('Total Volume','Expansion
Space','Compression Space')
grid on
hold off

% Velocity Check v. Time Plot
figure (4)
hold on
plot(time,v_check1,'-b','markersize',25);
plot(time,v_check2,'-r','markersize',25);
ylabel('Y Velocity (m/s)',"Fontsize",14)
xlabel('Time (s)',"Fontsize", 14)
legend('Interface 1','Interface 2')
grid on
hold off

% Force v. Time Plot
figure (5)
hold on
plot(time,F_displacer_upper,'-
b','markersize',25);
```

```
plot(time,F_displacer_lower,'-
r','markersize',25);
plot(time,F_powerpiston,'-g','markersize',25);
ylabel('Force (N)',"Fontsize",14)
xlabel('Time (s)',"Fontsize", 14)
legend('Displacer (upper)','Displacer
(lower)','Power Piston')
grid on
hold off

% PV Plot
figure (6)
plot(V_total,P_total,'-b','markersize',25);
ylabel('Pressure (Pa)',"Fontsize",14)
xlabel('Volume (m^3)',"Fontsize", 14)
grid on

%% Import Function
function Data1 = importfile(filename,
dataLines)
%IMPORTFILE Import data from a text file
%  DATA1 = IMPORTFILE(FILENAME) reads data from
text file FILENAME for
%  the default selection.  Returns the data as
a table.
%
%  DATA1 = IMPORTFILE(FILE, DATALINES) reads
data for the specified row
%  interval(s) of text file FILENAME. Specify
DATALINES as a positive
%  scalar integer or a N-by-2 array of positive
scalar integers for
%  dis-contiguous row intervals.
%
%  Example:
%  Data1 = importfile("C:\Users\2021\Documents\
MATLAB\Data1.out", [4, Inf]);
```

```
%
%  See also READTABLE.
%
% Auto-generated by MATLAB on 02-Jun-2022
11:21:32

%% Input handling

% If dataLines is not specified, define
defaults
if nargin < 2
   dataLines = [4, Inf];
end

%% Set up the Import Options and import the
data
opts =
delimitedTextImportOptions("NumVariables", 22);

% Specify range and delimiter
opts.DataLines = dataLines;
opts.Delimiter = " ";

% Specify column names and types
opts.VariableNames = ["TimeStep", "flow_time",
"max_pressure_channel",
"max_pressure_compression",
"max_pressure_expansion", "pressure_channel",
"pressure_compression", "pressure_expansion",
"temp_channel", "temp_compression",
"temp_expansion", "vol_avg_pressure_total",
"vol_avg_temp_total", "volume_compression",
"volume_expansion", "volume_total",
"y_force_displacer_bottom",
"y_force_displacer_top", "y_force_powerp",
"y_vel_avg_channel_compression_int",
"y_vel_avg_channel_expansion_int_",
"VarName22"];
```

```
opts.VariableTypes = ["double", "double",
"double", "double", "double", "double",
"double", "double", "double", "double",
"double", "double", "double", "double",
"double", "double", "double", "double",
"double", "double", "double", "string"];

% Specify file level properties
opts.ExtraColumnsRule = "ignore";
opts.EmptyLineRule = "read";
opts.ConsecutiveDelimitersRule = "join";
opts.LeadingDelimitersRule = "ignore";

% Specify variable properties
opts = setvaropts(opts, "VarName22",
"WhitespaceRule", "preserve");
opts = setvaropts(opts, "VarName22",
"EmptyFieldRule", "auto");

% Import the data
Data1 = readtable(filename, opts);

end
```

Figure 1

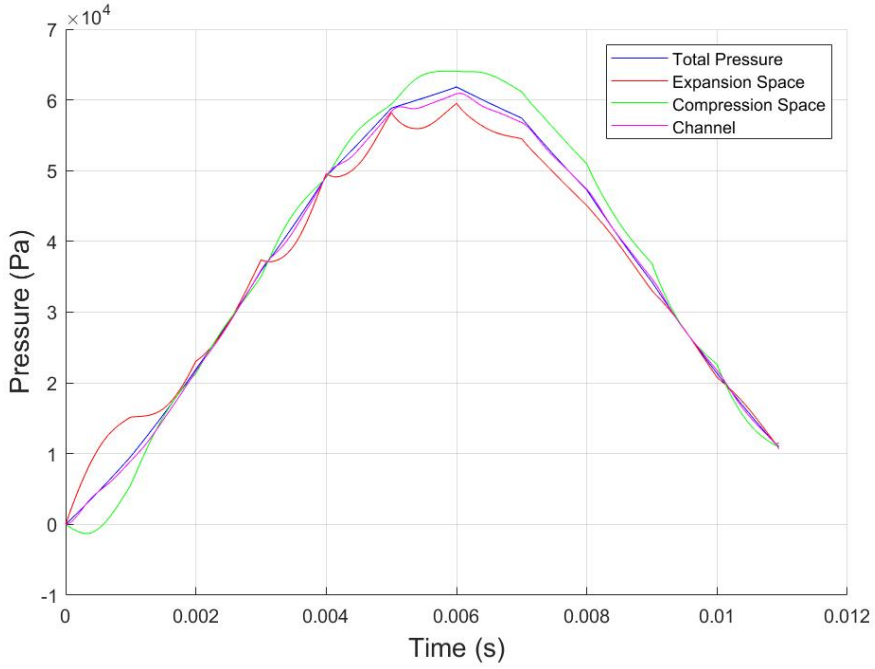

Figure 2

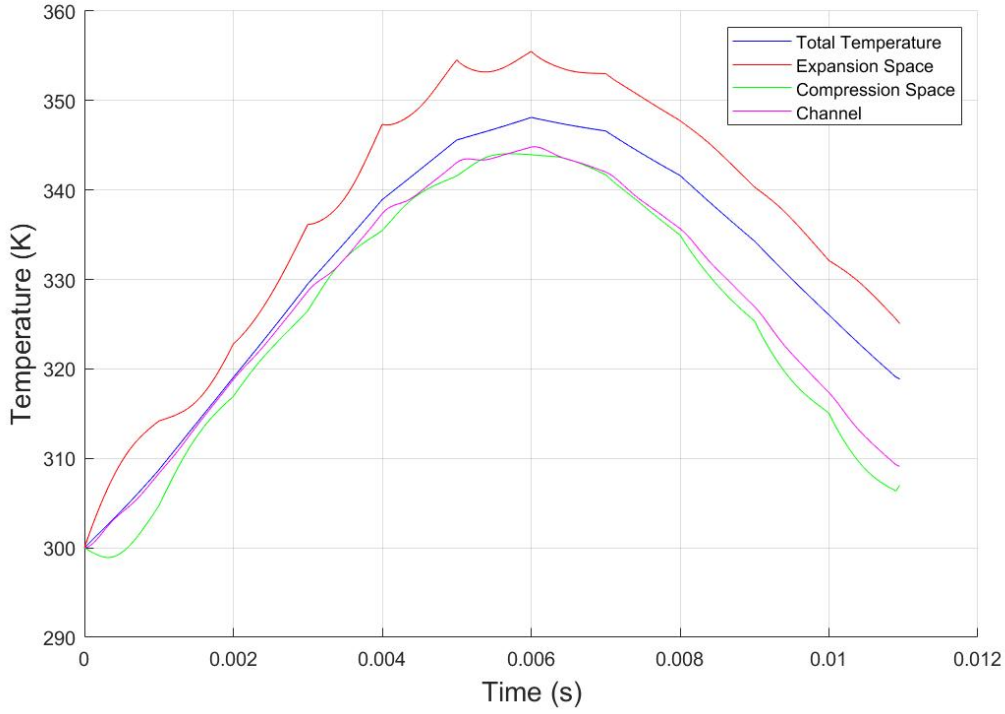

Figure 3

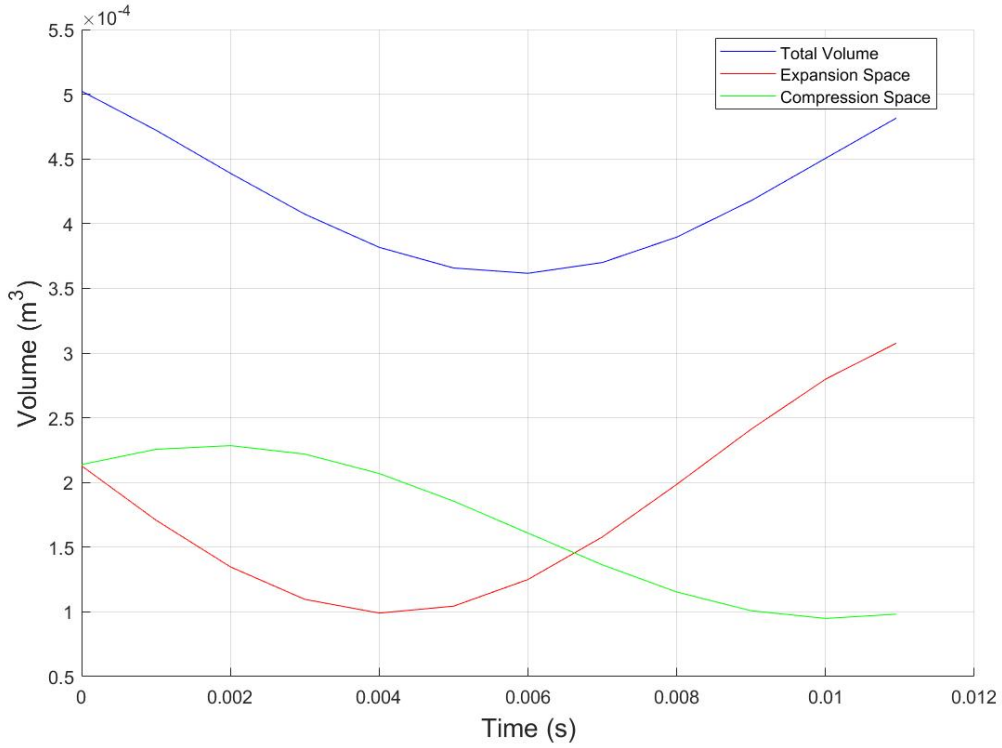

Figure 4

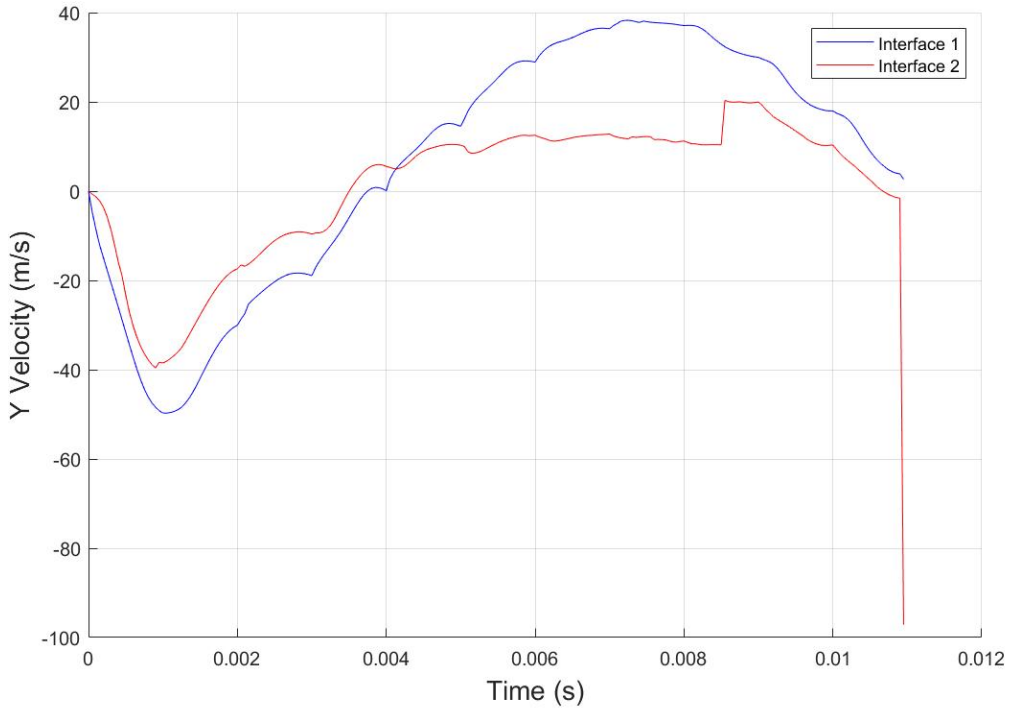

Figure 5

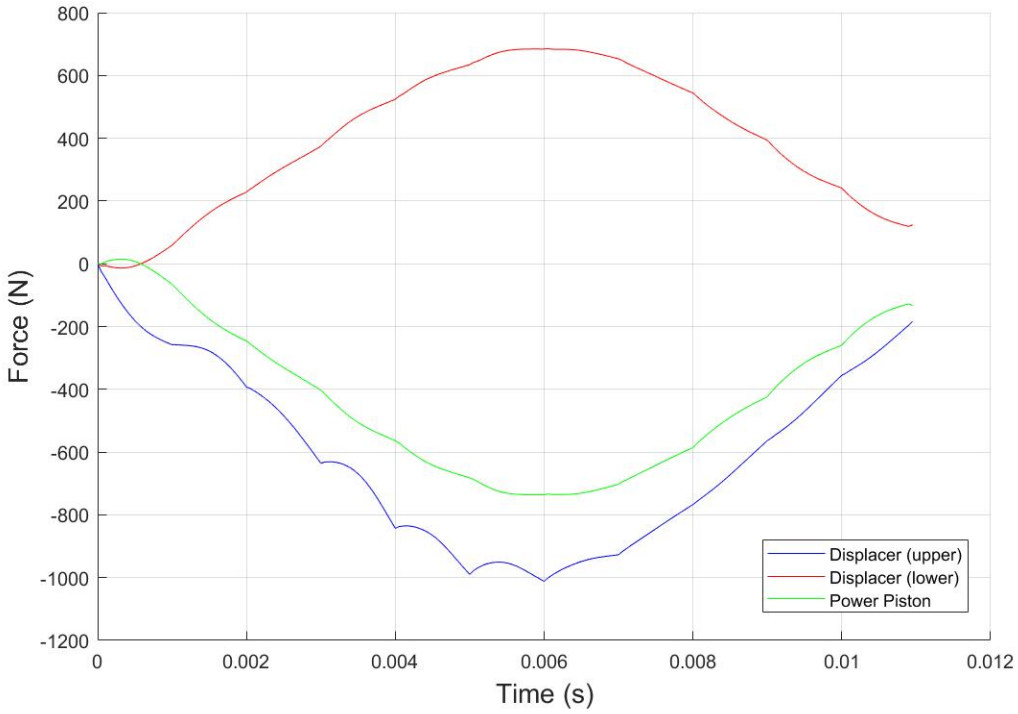
800
600
400
200
0
-200
-400
-600
-800
-1000
-1200
Force (N)
0
0.002
0.004
0.006
0.008
0.01
0.012
Time (s)
Displacer (upper)
Displacer (lower)
Power Piston

Figure 6

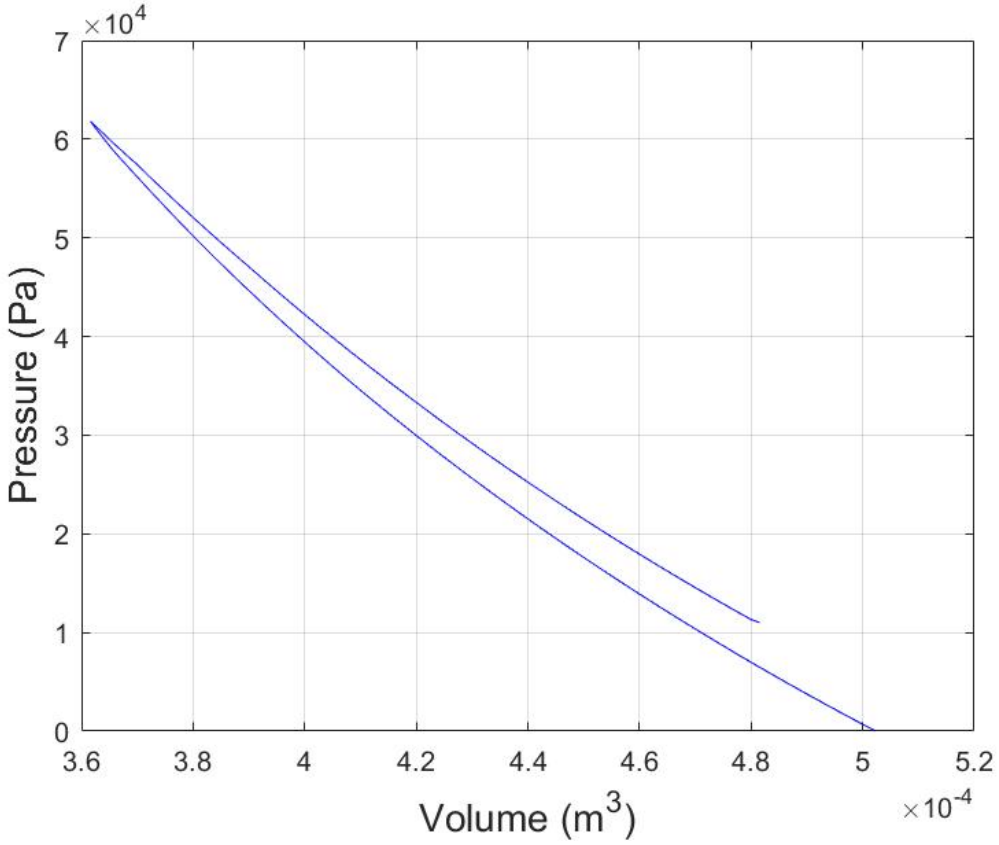
×10^4
7
6
5
4
3
2
1
0
Pressure (Pa)
3.6
3.8
4
4.2
4.4
4.6
4.8
5
5.2
Volume (m^3)
×10^-4

APPENDIX E. 3D-PRINTED HEAT SHIELD DIMENSIONS

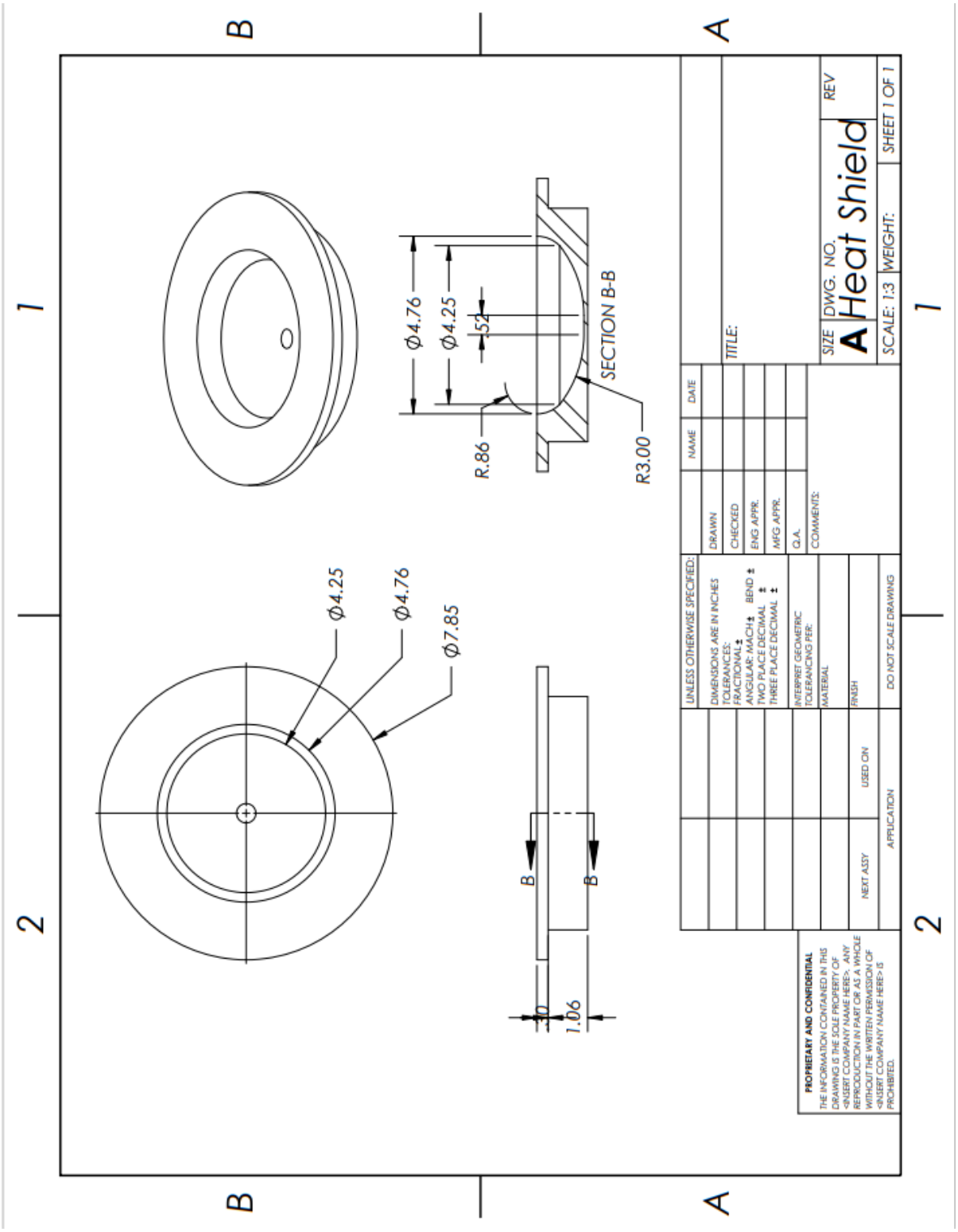

THIS PAGE INTENTIONALLY LEFT BLANK

APPENDIX F. MATLAB CODE FOR EXPERIMENTAL DATA PLOTS

Appendix F shows the MATLAB code that was used to plot Figures 27 through 30 in the main thesis body. It imports the output data from the controls box and data acquisition system.

```
% Experimental Data
close all, clc

% Temperature Defintions:
% T1 = Ambient
% T2 = Coolant Inlet
% T3 = Heater Head Surface
% T4 = Heat Acceptor
% T5 = Coolant Outlet
% T6 = Control Head
% T7 = Heater Head Ambient
% T8 = Level Head


% Trial 4: May17Run02
dataset4 =
importfile('StirlingDataMay17Run02.txt');
controlsbox4 = xlsread('Stirling Test 4 Data');
T1 = (dataset4{:,3}-32).*5./9;
T2 = (dataset4{:,4}-32).*5./9;
T3 = (dataset4{:,5}-32).*5./9;;
T4 = (dataset4{:,6}-32).*5./9;
T5 = (dataset4{:,7}-32).*5./9;
T6 = (dataset4{:,8}-32).*5./9;
T7 = (dataset4{:,9}-32).*5./9;
T8 = (dataset4{:,10}-32).*5./9;

%%
timestep = 0.02; %[s]
```

```
datapoints_4 = 45275;
time = [0:timestep:timestep*(datapoints_4-1)]';
duration = 85; %[s] calculated from recorded
video
adjustment = 15; %[s]
engine_stop = 330; %[s]
engine_start = engine_stop-duration; %[s]
engine_start = engine_start-adjustment; % add
15 seconds before the start
engine_stop = engine_stop+adjustment; % add 15
seconds after the stop
start = 50*engine_start+1; % time index for
engine start
stop = 50*engine_stop+1; % time index for
engine stop
time_total = (duration+adjustment*2)*50+1;

% For times with no adjustment:
time_total2 = duration*50+1;
engine_start2 = engine_start+adjustment;
engine_stop2 = engine_stop-adjustment;
start2 = 50*engine_start2+1; % time index for
engine start
stop2 = 50*engine_stop2+1; % time index for
engine stop

% 50*x+1 indices in 1 second
% Engine starts at about 243 seconds, plot at
235 seconds = index 11751
% Heater stops at 243+60 seconds = 303 seconds
= index 15151
% Engine stops at 330 seconds. Plot to 340
seconds = index 17001
% Engine runs for 87, plotting for 105 s = 5251
indices
```

```
%-------------------------------------------------
---------------------------

% External Data
figure (1)
hold on
yyaxis left
plot(time(1:time_total,:),T1(start:stop),'-
b','markersize',.5); % T1 ambient temperature
plot(time(1:time_total,:),T2(start:stop),'-
c','markersize',8); % T2 coolant inlet
plot(time(1:time_total,:),T5(start:stop),'-
g','markersize',8); % T5 coolant outlet
plot(time(1:time_total,:),T3(start:stop), '-
k','markersize',8); % T3 heater head surface
plot(time(1:time_total,:),T4(start:stop),'-
r','markersize',8); % T4 heat acceptor
plot(time(1:time_total,:),T6(start:stop),'-
m','markersize',.5); % T6 control head
plot(time(1:time_total,:),T8(start:stop),'-
y','markersize',.5); % T8 level head
plot(time(1:time_total,:),T7(start:stop),'--
r','markersize',8); % T7 heater head ambient
ylabel('Temperature (C)',"Fontsize",14)
yyaxis right
plot((controlsbox4(:,2)+adjustment+2),controlsb
ox4(:,3),'.-k','markersize',10)% Power
xlabel('Time (s)',"Fontsize", 14)
ylabel('Power (W)', "Fontsize", 14)
legend('Ambient','Coolant Inlet','Coolant
Outlet','Heater Head Surface','Heat
Acceptor','Control Head (External)','Level Head
(External)','Heater Head Ambient',"Power")
grid on
hold off

% Controls box data
```

```
figure (2)
plot(controlsbox4(:,2),controlsbox4(:,6),'m','m
arkersize',8) % Head Control T
hold on
yyaxis left
plot(controlsbox4(:,2),controlsbox4(:,8),'-
c','markersize',8) % Coolant Inlet T
plot(controlsbox4(:,2),controlsbox4(:,9),'-
g','markersize',8) % Coolant Outlet T
plot(controlsbox4(:,2),controlsbox4(:,10),'-
r','markersize',8) % Back End T
plot(controlsbox4(:,2),controlsbox4(:,11),'-
b','markersize',8) % Ambient T
ylabel('Temperature (C)',"Fontsize",14)
yyaxis right
plot(controlsbox4(:,2),controlsbox4(:,3),'.-
k','markersize',8) % Power
xlabel('Time (s)',"Fontsize", 14)
ylabel('Power (W)', "Fontsize", 14)
legend('Head Control','Coolant Inlet','Coolant
Outlet','Back End','Ambient','Power')
grid on
hold off

% TH-TC v. Power
figure (3)
plot(controlsbox4(:,14),controlsbox4(:,3),'.b',
'markersize',15)
hold on
xlabel('TH-TC (C)',"Fontsize",14)
ylabel('Power (W)',"Fontsize",14)
grid on
hold off


% Head control v. Power
figure (4)
```

```
plot(controlsbox4(:,6),controlsbox4(:,3),'.')
xlabel('Head Control Temperature (C)')
ylabel('Power (W)')

% Combined Data

figure (6)
% Redundant temperatures
plot(controlsbox4(:,2),controlsbox4(:,6),'.b','
markersize',8) % head control
hold on
plot(time(1:time_total2,:),T6(start2:stop2),'-
b','linewidth',1);

plot(controlsbox4(:,2),controlsbox4(:,8),'.r','
markersize',8) % coolant inlet
plot(time(1:time_total2,:),T2(start2:stop2),'-
r','linewidth',1);

plot(controlsbox4(:,2),controlsbox4(:,9),'.g','
markersize',8) % coolant outlet
plot(time(1:time_total2,:),T5(start2:stop2),'-
g','linewidth',1);
xlabel('time (s)','Fontsize',14)
ylabel('Temperature (C)','Fontsize', 14)
legend("Head Control (Thermocouple)","Head
Control (Controls Box)","Coolant Inlet
(Thermocouple)","Coolant Inlet (Controls
Box)","Coolant Outlet (Thermocouple)","Coolant
Outlet (Controls Box)","Fontsize",8)
grid on
hold off

% head delta T v.Time
figure (7)
plot(controlsbox4(:,2),controlsbox4(:,6),'.-
b','markersize',8)
hold on
```

```
yyaxis left
plot(controlsbox4(:,2),controlsbox4(:,14),'.-
g','markersize',8)
plot(controlsbox4(:,2),controlsbox4(:,7),'.-
c','markersize',8)
ylabel('Temperature (C)',"Fontsize",14)
yyaxis right
plot(controlsbox4(:,2),controlsbox4(:,3),'.-
k','markersize',8)
xlabel('Time (s)',"Fontsize", 14)
ylabel('Power (W)', "Fontsize", 14)
legend('Head Control','TH-TC','Head Delta
T','Power')
grid on
hold off

%% Presentation Plots
% External Data
figure (8)
hold on
yyaxis left
plot(time(1:time_total,:),T4(start:stop),'-
r','markersize',9); % T4 heat acceptor
plot((controlsbox4(:,2)+adjustment+2),controlsb
ox4(:,6),'-m','markersize',9) % Head Control T
plot(time(1:time_total,:),T1(start:stop),'-
b','markersize',9); % T1 ambient temperature
plot(time(1:time_total,:),T2(start:stop),'-
c','markersize',9); % T2 coolant inlet
plot(time(1:time_total,:),T5(start:stop),'-
g','markersize',9); % T5 coolant outlet
ylabel('Temperature (C)',"Fontsize",14)
yyaxis right
plot((controlsbox4(:,2)+adjustment+2),controlsb
ox4(:,3),'.-k','markersize',10)% Power
xlabel('Time (s)',"Fontsize", 14)
ylabel('Power (W)', "Fontsize", 14)
```

```
legend('Heat Acceptor','Head Control
T','Ambient','Coolant Inlet','Coolant
Outlet','Power')
grid on
hold off

% Head control v. delta T head

% head delta T v.Time
figure (9)
plot(time(1:time_total,:),T4(start:stop),'-
r','markersize',8); % T4 heat acceptor
hold on
yyaxis left
plot(controlsbox4(:,2),controlsbox4(:,6),'.-
b','markersize',8) % Head control
plot(controlsbox4(:,2),controlsbox4(:,7),'.-
c','markersize',8) % Head Delta T
ylabel('Temperature (C)',"Fontsize",14)
yyaxis right
plot(controlsbox4(:,2),controlsbox4(:,3),'.-
k','markersize',8) % Power
xlabel('Time (s)',"Fontsize", 14)
ylabel('Power (W)', "Fontsize", 14)
legend('Heat Acceptor','Head Control','Head
Delta T','Power')
grid on
hold off

%% DATA IMPORT FUNCTION
function StirlingDataMay17Run02 =
importfile(filename, dataLines)
%IMPORTFILE Import data from a text file
%  STIRLINGDATAMAY17RUN02 =
IMPORTFILE(FILENAME) reads data from text
%  file FILENAME for the default selection.
Returns the data as a table.
```

```
%
%  STIRLINGDATAMAY17RUN02 = IMPORTFILE(FILE,
DATALINES) reads data for
%  the specified row interval(s) of text file
FILENAME. Specify
%  DATALINES as a positive scalar integer or a
N-by-2 array of positive
%  scalar integers for dis-contiguous row
intervals.
%
%  Example:
%  StirlingDataMay17Run02 =
importfile("C:\Users\2021\Documents\MATLAB\
StirlingDataMay17Run02.txt", [1, Inf]);
%
%  See also READTABLE.
%
% Auto-generated by MATLAB on 17-May-2022
19:45:14

%% Input handling

% If dataLines is not specified, define
defaults
if nargin < 2
   dataLines = [1, Inf];
end

%% Set up the Import Options and import the
data
opts =
delimitedTextImportOptions("NumVariables", 19);

% Specify range and delimiter
opts.DataLines = dataLines;
opts.Delimiter = ["\t", " "];

% Specify column names and types
```

```
opts.VariableNames = ["Date", "Var2", "Time",
"T1", "T2", "T3", "T4", "T5", "T6", "T7", "T8",
"Var12", "Var13", "Var14", "Var15", "Var16",
"Var17", "Var18", "Var19"];
opts.SelectedVariableNames = ["Date", "Time",
"T1", "T2", "T3", "T4", "T5", "T6", "T7",
"T8"];
opts.VariableTypes = ["datetime", "string",
"string", "double", "double", "double",
"double", "double", "double", "double",
"double", "string", "string", "string",
"string", "string", "string", "string",
"string"];

% Specify file level properties
opts.MissingRule = "omitrow";
opts.ExtraColumnsRule = "ignore";
opts.EmptyLineRule = "read";

% Specify variable properties
opts = setvaropts(opts, ["Var2", "Time",
"Var12", "Var13", "Var14", "Var15", "Var16",
"Var17", "Var18", "Var19"], "WhitespaceRule",
"preserve");
opts = setvaropts(opts, ["Var2", "Time",
"Var12", "Var13", "Var14", "Var15", "Var16",
"Var17", "Var18", "Var19"], "EmptyFieldRule",
"auto");
opts = setvaropts(opts, "Date", "InputFormat",
"MM/dd/yyyy");

% Import the data
StirlingDataMay17Run02 = readtable(filename,
opts);

end
```

THIS PAGE INTENTIONALLY LEFT BLANK

LIST OF REFERENCES

[1] U.S. Energy Information Administration, "Short-Term Energy Outlook," *U.S. Energy Information Administration Independent Statistics and Analysis*, Apr. 12, 2022. https://www.eia.gov/outlooks/steo/report/electricity.php

[2] The White House, "FACT SHEET: President Biden Sets 2030 Greenhouse Gas Pollution Reduction Target Aimed at Creating Good-Paying Union Jobs and Securing U.S. Leadership on Clean Energy Technologies," *The White House Statements and Releases*, Apr. 22, 2021. https://www.whitehouse.gov/briefing-room/statements-releases/2021/04/22/fact-sheet-president-biden-sets-2030-greenhouse-gas-pollution-reduction-target-aimed-at-creating-good-paying-union-jobs-and-securing-u-s-leadership-on-clean-energy-technologies/

[3] A. Moreno, "The United States' Clean Energy Goals." https://www.renewable-ei.org/pdfdownload/activities/01_Key_AlejandroMoreno.pdf

[4] Center for Climate and Energy Solutions, "Microgrids," *Center for Climate and Energy Solutions*, Oct. 16, 2017. https://www.c2es.org/content/microgrids/

[5] G. Walker and J. R. Senft, "The Sunpower Engines," in *Free Piston Stirling Engines*, vol. 12, Berlin, Heidelberg: Springer Berlin Heidelberg, 1985, pp. 128–144. https://doi.org/10.1007/978-3-642-82526-2_4.

[6] H. Ibrahim, A. Ilinca, and J. Perron, "Energy Storage Systems—Characteristics and Comparisons," *Renew. Sustain. Energy Rev.*, vol. 12, no. 5, pp. 1221–1250, Jun. 2008, https://doi.org/10.1016/j.rser.2007.01.023.

[7] A. Boyden, V. K. Soo, and M. Doolan, "The Environmental Impacts of Recycling Portable Lithium-Ion Batteries," *Procedia CIRP*, vol. 48, pp. 188–193, 2016, https://doi.org/10.1016/j.procir.2016.03.100.

[8] C. Perozziello, L. Grosu, and B. M. Vaglieco, "Free-Piston Stirling Engine Technologies and Models: A Review," *Energies*, vol. 14, no. 21, p. 7009, Oct. 2021, https://doi.org/10.3390/en14217009.

[9] I. Urieli, "Chapter 3: The First Law of Thermodynamics for Closed Systems," *University of Ohio*. https://www.ohio.edu/mechanical/thermo/Intro/Chapt.1_6/Chapter3b.html

[10] C. Girouard, "Model-Based and Experimental Analysis for Future Liquid Air Energy Storage Systems," Naval Postgraduate School, Monterey, CA, 2019.

[11] W. Beale, *Understanding Stirling Engines*. Arlington: Volunteers in Technical Assistance, 1984.

[12] C. Woodford, “Stirling Engines,” *Explain That Stuff*, May 28, 2021. https://www.explainthatstuff.com/how-stirling-engines-work.html

[13] G. Walker, “The Stirling Engine,” *Sci. Am.*, vol. 229, no. 2, pp. 80–87, Aug. 1973.

[14] J. Egas and D. Clucas, “Stirling Engine Configuration Selection,” *Energies*, vol. 11, no. 3, p. 584, Mar. 2018, https://doi.org/10.3390/en11030584.

[15] A. S. Nielson, “Enhancing the Effectiveness of Stirling Regenerators,” University of Ontario Institute of Technology, Oshawa, Ontario, Canada, 2019.

[16] A. Asnaghi, S. M. Ladjevardi, P. Saleh Izadkhast, and A. H. Kashani, “Thermodynamics Performance Analysis of Solar Stirling Engines,” *ISRN Renew. Energy*, vol. 2012, pp. 1–14, Jul. 2012, https://doi.org/10.5402/2012/321923.

[17] W. T. Beale, “Self-Starting, Free Piston Stirling Engine,” 4036018, Jul. 19, 1977

[18] W. T. Beale, “Stirling Cycle Type Thermal Device,” RE30176, Dec. 25, 1979

[19] S. Qiu and L. Solomon, “Free-Piston Stirling Engine Generators,” in *Energy Conversion - Current Technologies and Future Trends*, I. H. Al-Bahadly, Ed. IntechOpen, 2019. https://doi.org/10.5772/intechopen.79413.

[20] N. C. J. Chen and F. P. Griffin, “Review of Stirling-Engine Mathematical Models,” ORNL/CON-135, 5948203, Aug. 1983. https://doi.org/10.2172/5948203.

[21] A. Ridha, A. Mohamed, C. Boualem, and K. Tayeb, “Two-Dimensional CFD Simulation Coupled With 6DOF Solver For Analyzing Operating Process of Free Piston Stirling Engine,” *J. Adv. Res. Fluid Mech. Therm. Sci.*, vol. 55, no. 1, pp. 29–38, 2019.

[22] C. C. Kwasi-Effah, A. I. Obanor, F. A. Aisien, and O. Ogbeide, “Review of Existing Models for Stirling Engine Performance Prediction and the Paradox Phenomenon of the Classical Schmidt Isothermal Model,” *Int. J. Energy Sustain. Dev.*, vol. 1, no. 1, pp. 6–12, 2016.

[23] I. Urieli, “Stirling Engine Ideal Isothermal Analysis,” *University of Ohio*. https://www.ohio.edu/mechanical/stirling/isothermal/isothermal.html

[24] I. Urieli, “Stirling Engine Ideal Adiabatic Analysis,” *University of Ohio*. https://www.ohio.edu/mechanical/stirling/adiabatic/adiabatic.html

[25] I. Urieli and D. M. Berchowitz, *Stirling Cycle Engine Analysis*. Bristol: Adam Hilger, 1984. [Online]. Available: https://www.osti.gov/etdeweb/biblio/6068495

[26] N. A. M. Rasli and S. Saadon, “CFD Analysis of Heat Transfer Through Stirling Engine with Different Regenerators,” *J. Adv. Res. Fluid Mech. Therm. Sci.*, vol. 64, no. 1, pp. 126–134, 2019.

[27] J. G. M. Saturno, “Some Mathematical Models to Describe the Dynamic Behavior of the B-10 Free-Piston Stirling Engine.” 1994.

[28] K. Wang, S. R. Sanders, S. Dubey, F. H. Choo, and F. Duan, “Stirling Cycle Engines For Recovering Low and Moderate Temperature Heat: A Review,” *Renew. Sustain. Energy Rev.*, vol. 62, pp. 89–108, Sep. 2016, https://doi.org/10.1016/j.rser.2016.04.031.

[29] P. Durcansky, R. Nosek, and J. Jandacka, “Use of Stirling Engine for Waste Heat Recovery,” *Energies*, vol. 13, no. 16, p. 4133, Aug. 2020, https://doi.org/10.3390/en13164133.

[30] S. Zhu *et al.*, “A Free-Piston Stirling Generator Integrated with a Parabolic Trough Collector for Thermal-To-Electric Conversion of Solar Energy,” *Appl. Energy*, vol. 242, pp. 1248–1258, May 2019, https://doi.org/10.1016/j.apenergy.2019.03.169.

[31] A. Mabe, H. Takami, and F. Ishibashi, “Biomass Free Piston Stirling Engine Generator with PV,” in *2018 7th International Conference on Renewable Energy Research and Applications (ICRERA)*, Paris, Oct. 2018, pp. 561–566. https://doi.org/10.1109/ICRERA.2018.8566744.

[32] N. Bailey, “Model-Based Simulation, Analysis, and Prototyping for Future Liquid Air Energy Storage Systems,” Naval Postgraduate School, Monterey, CA, 2019.

[33] N. Bailey, C. Girouard, and A. Pollman, “Dual Stirling Cycle Liquid Air Battery” [Online]. Available: https://patents.google.com/patent/US20220042478A1/en?oq=17%2f393%2c275

[34] T. Howe, A. Pollman, and A. Gannon, “Operating Range for a Combined, Building-Scale Liquid Air Energy Storage and Expansion System: Energy and Exergy Analysis,” *Entropy*, vol. 20, no. 10, p. 770, Oct. 2018, https://doi.org/10.3390/e20100770.

THIS PAGE INTENTIONALLY LEFT BLANK

INITIAL DISTRIBUTION LIST

1. Defense Technical Information Center
   Ft. Belvoir, Virginia

2. Dudley Knox Library
   Naval Postgraduate School
   Monterey, California